CMOS ANALOG CORRELATOR BASED GLUCOSE SENSOR READOUT CIRCUIT

by

VARUN SHENOY

Presented to the Faculty of the Graduate School of

The University of Texas at Arlington in Partial Fulfillment

of the Requirements

for the Degree of

DOCTOR OF PHILOSOPHY

THE UNIVERSITY OF TEXAS AT ARLINGTON

May 2013

Acknowledgements

First and foremost, with immense gratitude, I would like to acknowledge the support and help of my advisor, Dr. Sungyong Jung. I am indebted to him for his guidance and continuous support of my Ph.D. study and research, and for his patience and motivation. I have learnt a lot about research and its principles from him over these years, which will always be with me throughout my life along with his friendship.

I would also like to thank Dr. Lee, Dr. Zhou, Dr. Davoudi and Dr. Gao for being my dissertation defense committee members. I would like to give a special thanks to Dr. Davoudi for lending us with equipment which aided in my research. I want to mention the electrical engineering department assistants, Gail, Ann, and Janice for their constant and kind assistances.

I wish to thank my fellow former/current AMIC lab members: Tim, JC, Niranjan, Sunil and Sujith for all their invaluable inputs to my research and for being good friends to help create a great environment for research and discussion in the lab. You all add so many positive things and great memories into my research experiences.

Finally and most importantly, this dissertation would not be possible without the love and support of my family and friends. My parents and my wife are my biggest strength and I thank them from the bottom of my heart and dedicate this work to them.

April 09, 2013

Abstract

CMOS ANALOG CORRELATOR BASED

GLUCOSE SENSOR

READOUT CIRCUIT

Varun Shenoy, PhD

The University of Texas at Arlington, 2013

Supervising Professor: Sungyong Jung

Recent investigations show research and development of alternative methods of glucose sensing using electrochemical biosensors to help significantly reduce the difficulties associated with treating diabetes. The integration of microelectronic circuit technology with biosensors is generating greater research interest. The advantages of small size and less power consumption of integrated circuits (ICs) are helping with the realization of biosensors for improved performance. The major challenges involving designing of readout ICs for the electrochemical biosensors are accuracy and range.

In this research work, an analog correlator based readout circuit for amperometric glucose electrochemical biosensors is designed and implemented. It is designed to work with the output range of a novel microneedle based non-enzymatic painless glucose sensor. This minimally invasive sensor is designed to measure the glucose level of the interstitial fluid in epidermis layer. The analog correlator based readout circuit can achieve the required input current range (5µA to 30µA) from the microneedle based glucose sensor and show a linear output in that range. The analog correlator based glucose sensor readout circuit offers lower noise and wider dynamic range compared to the conventional TIA architecture and is a better solution for the readout circuit for the microneedle based sensor.

For the CMOS IC implementation, the analog correlator based readout circuit is designed and fabricated in 0.35um CMOS process. The design and analysis of the individual circuit components including the op-amp and multiplier are presented in this work. The op-amp achieves a 118.3 dB gain and 47.3 degrees phase margin. The circuit DC response for input range of 5uA to 30uA gives a linear output voltage range from 0.21V to 1.38V. The total output RMS noise is simulated to be 6.6mV_{RMS}. The circuit has a mean error of 1.6% and consumes 5.1mW of power. The total area of the proposed readout circuit is 300um × 167um.

Table of Contents

List of Illustrations

List of Tables

Chapter 1

Introduction

Electrochemical sensing system, like other areas, is moving towards development of small, accurate and affordable devices. Integrated circuit(IC) and advancement in micro electro-mechanical systems (MEMS) technology has made this possible and will allow health care, medicine and biological science products indispensable parts of lifestyle besides computers, cell phones, digital cameras and many other devices.

The amalgamation of capabilities of integrated circuit to detect and process biosensor signals, and micro-machined sensors and actuators has provided a great opportunity for researchers to explore and analyze the realms, for example, of processing neural signals, communicate with neurons, measure blood pressure, examine biological and physiological signals, and many more applications.

This thesis explores the application of integrated circuit design, to measure the response of a microneedle-based non-enzymatic glucose sensor used in a continuous blood glucose monitoring type system. In this chapter, the motivation for glucose sensing system with a background of diabetes, hyperglycemia, and hypoglycemia and then types of glucose sensing techniques in glucose sensing are reviewed. The research objectives for this dissertation are described.

Diabetes is the most common endocrine disorder of the metabolism of carbohydrate, fat and protein and is associated with an insufficiency of insulin secretion [1]. Insulin is a hormone which is released from pancreas to regulate the amount of glucose in the bloodstream. It improves the entry of glucose into liver, muscle and adipose tissue and to promote storage of energy substrate in the form of glycogen and

protein resulting in lowering of the blood glucose concentration. Therefore, when the pancreas doesn't produce the correct level of insulin the symptoms of diabetes occur [2].

There are two types of diabetes. Type-1 diabetes occurs when the insulin-producing cells of the pancreas are destroyed by chronic immune system resulting in serious problems with eye (ret, kidney and peripheral nerves. Type-1 diabetic patients have absolute insulin deficiency and it can be treated by insulin injection in the subcutaneous tissues of arms, legs and abdomen to normalize the blood glucose concentration and patients need to monitor their blood glucose level regularly by means of common finger-stick type blood glucose monitoring device. It is estimated that 5 ~ 10 % of Americans who are diagnosed with diabetes have Type-1 diabetes [3].

In Type-2 diabetic patients, organs are less sensitive to insulin and the production of insulin by pancreatic cells isn't enough as the insulin is not used as it should be. Therefore, glucose can't get into the body's cells appropriately and it is reported that approximately 285 million adults (age between 20 and 79) suffer from Type-1 and/or Type-2 diabetes and this number is expected to increase to 430 million adults by 2030 [4].

In the last few decades home glucose testing has evolved to assist people with types 1 and 2 diabetes to overcome the daily challenge of maintaining a stable glucose level in their body. It provides the person with diabetes a glucose reading at that particular moment in time and also because of the inconvenience of pricking finger to make a glucose measurement, the person with diabetes often performs testing less than twice per day. The different conditions of Blood Glucose levels are:

- Euglycemia – between 4mmol/l to 7mmol/l
- Hyperglycemia – above 7mmol/l
- Hypoglycemia – below 4mmol/l

Very low glucose concentration (<4mmol/l) is called hypoglycemia, which may cause fainting, coma and even death. Very high glucose concentration (>7mmol/l) or hyperglycemia over time can cause damages to the eyes, kidney, nerves, and blood vessels0020y1 [5]. During sleep a person with diabetes cannot maintain the state of euglycemia (blood glucose between 4mmol/l - 7mmol/l).

Glucose sensors may be invasive, non-invasive or minimally invasive and may use transdermal technologies or sampling of blood or interstitial fluid (ISF) [6]. Interstitial fluid is a small-volume compartment of fluid that surrounds the cells, glucose enters this from blood and is removed once the cells within the compartment consume glucose available. Glucose concentrations in the ISF are a function of blood flow, metabolic rate and the rate of change of glucose concentration in blood. Studies suggest that Glucose concentration in ISF lags blood by 6.7min [7] but ISF responds faster than blood for reducing glucose concentrations and hence can be used for early warning of hypoglycemia [8].

(1) Invasive glucose sensors

Subcutaneous needle - type sensors measure glucose concentration in blood using enzyme electrodes which catalyze reduction-oxidation (redox) reactions that cause electrons to flow. Most of the commercially available glucose-sensing systems are based on subcutaneous needle-type amperometric glucose oxidase (GOx) enzyme electrodes.

(2) Minimally-invasive glucose sensors

Micropore techniques puncture the stratum corneum without penetrating the full thickness of skin by applying pulsed laser or by the local application of heat and extracts ISF by vacuum [9].

Microneedle based system has often been cited as inspired by female mosquito's blood sampling ability [10]. Hollow microneedles (175µm thickness) are used to sample

200nl of capillary blood using capillary forces. The penetration of these needles is painless and sampled blood can be analyzed using an enzyme-based [11] or non-enzyme- based [12] electrode system.

(3) Non-invasive glucose sensors

Transdermal techniques are non-invasive as they do not breach the skin, but use physical energy to access ISF or blood and extract glucose. Optical techniques analyze the properties of reflected or scattered light to estimate light in the ISF or in the anterior chamber of the eye [6].

Most common method of blood glucose monitoring is through sampling of small amount of blood at the patient's finger tip using a tiny lancet. Frequent blood sampling from finger tip creates trypanophobia for many diabetes patients. There have been numerous investigations to develop alternative methods of blood glucose monitoring to avoid frequent blood sampling from finger tip, including sampling from alternate sites other than finger tip, wireless glucose sensor [13], etc. MEMS technologies can provide a variety of options for painless blood glucose monitoring [14], and recent advances in microneedles [15] are ideally suited to provide options of painless blood sampling.

Design and implement a glucose sensing integrated readout circuit using CMOS process to detect current from a micro-needle non-enzymatic glucose sensor. The CMOS readout circuit should achieve the required input current range and show a linear output in that range. The circuit should also exhibit low noise to achieve a wide dynamic range.

This thesis is organized into five chapters:

Chapter 1 presents the motivation for glucose sensing system with a background of diabetes, hyperglycemia, and hypoglycemia and then types of glucose sensing techniques in glucose sensing are reviewed. The research objectives for this dissertation are described.

Chapter 2 provides a review of electrochemistry, electrochemical sensors and its classifications, electrochemical glucose sensors and its evolution. The electrical equivalent sensor model is also discussed.

Chapter 3 presents a background for microneedles and their application in painless glucose sensing. The microneedle-based non-enzymatic sensor considered for this work is introduced.

Chapter 4 provides the design of the proposed analog correlator based glucose sensing readout circuit. It first shows a PCB implementation of the proposed circuit glucose sensing system done with commercial off-the-shelf component. Then a IC implementation of the proposed circuit in 0.35 um CMOS process is discussed with simulation and measurement results.

Chapter 5 concludes this thesis with the contribution of this work and a set of future research objectives that can be conducted to improve the results of this thesis.

Chapter 2

Background

2.1 Electrochemistry

Electrochemistry is based on Faraday's discovery of equivalence that exists between electricity and chemistry. The electrode in a solution performs the role of a transducer between the chemical and electrical domains by either monitoring the chemical components in the solution or by generating new chemical components that will interact with the medium in a measurable way.

Electrochemical reactions occur in a medium containing dissolved ions (electrolyte) which aid the current flow. Usually, the solvent-electrolyte combination chosen for use in electrochemical experiments are strong electrolytes (fully broken down into ions when dissolved in solvent). Current flow between the electrodes in electrochemical cells is a function of solution resistance of the electrolyte between the electrodes. The value of this resistance depends on the ionic conductivity of the electrolyte, and also on the geometric arrangement of electrodes in the cell [16].

Generally, description of the chemical reaction can be inferred by observing the voltage-current characteristic of an electrode/solution and relating it to the system knowledge. Hence, most of the electrochemistry methods deal with the interrelation between interfacial potential differences and thermodynamics of electrode reactions.

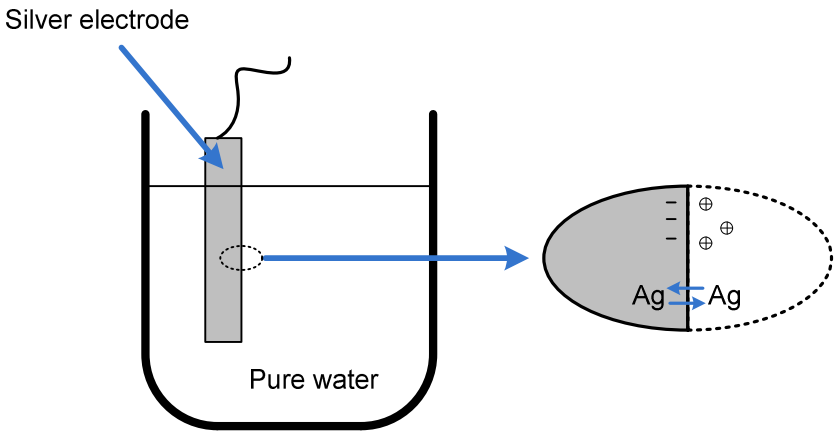

Figure 2.1 Oxidation of a silver electrode immersed in pure water.

As an example, if a silver electrode immersed in pure water (Figure 2.1) some of the silver atoms dissolve in the solution (water) as positive ions (Ag+), leaving their electrons in the electrode based on the following equation:

$$Ag \rightarrow Ag^{+} + e^{-} \quad (1)$$

The buildup of charge in the electrode and the solution causes an interfacial potential difference, which can affect the rate and direction of the reaction. Different electrodes have different interfacial potential differences.

The two basic types of charge transfer reactions take place at an electrode solution interface: oxidation and reduction. During an oxidation reaction, the chemical species transfer electron(s) to the electrode, while in a reduction reaction; the chemical species receive electron(s) from the electrode. The resulting chemical reactions are represented as:

Oxidation:

$$R \rightarrow O + ne^{-} \quad (2)$$

Reduction:

$$O + ne^{-} \rightarrow R \quad (3)$$

where O is the oxidized species, R is the reduced form of species and n is the number of electrons transferred during the reaction.

Interfacial potential differences across a very short difference corresponding to a thin layer of electrolyte attached to the electrode surface are restricted to a few volts. Thus, a very large potential gradient exists on the electrode/electrolyte interface.

The interfacial potential difference, E, of an electrode can be calculated using the Nernst equation [9]:

$$E = E^0 + \frac{RT}{nF} ln\left(\frac{C_o}{C_R}\right) \quad (4)$$

where E^0 is the standard potential of the electrode, R is the molar gas constant, T is temperature, F is Faraday's constant and C_o and C_R are the concentration of the oxidized and reduced forms of the species, respectively [16].

2.2 Electrochemical Cell

Electrochemical cells are broadly divided into two sub-types, galvanic and electrolytic. In galvanic cells the reactions start spontaneously when the electrodes are connected via a conductor, while on the other hand an electrolytic cell (Figure 2.2) requires a potential in excess of its operating cell potential (OCP) to be applied in order to drive an electrochemical process.

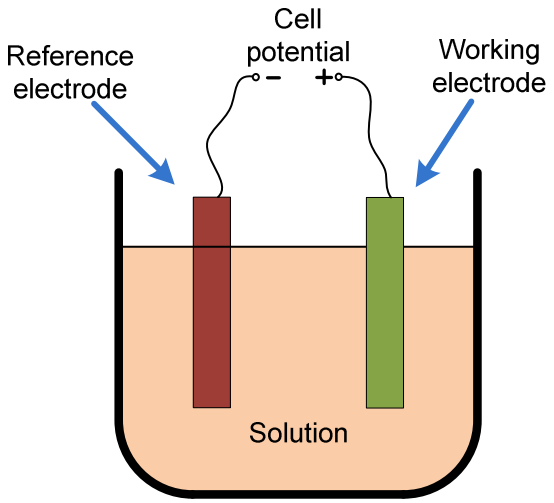

Figure 2.2 A simple electrochemical cell.

The electrodes are identified by the function they perform in the cell: the working electrode (WE), the reference electrode (RE) [16]. The overall chemical reaction occurring in an electrochemical cell consists of two independent half-reactions describing the real chemical changes at each of the two electrodes. Each half-reaction responds to the interfacial potential difference at the corresponding electrode.

The WE is generally a cathode which experiences the reaction of interest. WE can be chemically modified in order to increase its sensitivity to observe a specific species or to decrease the potential required to drive a particular reaction.

The RE is typically an anode, it must retain a constant composition and provide a stable potential by which the WE potential can be monitored. RE behave similarly to ideal non-polarizable electrodes. Such electrodes, depending on the external applied potential, can easily transfer charges across its interface with the solution, and its interfacial potential does depend on the flowing current. A more common reference electrode is the silver-silver chloride (Ag/AgCl) electrode. Saturated calomel electrode (SCE) is used as a reference electrode in this work [12].

2.2.1 Faradaic and Non-faradaic Process

The current flow at an electrode/electrolyte interface is mainly due to two kinds of processes faradaic and Non-faradaic. In faradaic process the charges are transferred at the electrode/electrolyte interface due to oxidation or reduction reactions. Therefore the resulting current is called faradaic current, and the electrodes through which this current flow is called charge-transfer electrodes. This depends mostly on two factors [16], [17]:

1. The rate at which the material moves from the bulk of the electrolyte to the electrode surface (this is called mass transfer).
2. The rate at which electrons transfer from the electrode to electrolyte and vice versa (this is called charge transfer).

Non-faradaic processes, such as adsorption and desorption can cause a transient current flow through the interface when the potential, electrode area, or solution composition changes [9]. Therefore in an ideal sensor, the sensor current should have only the faradaic component and the non-faradaic component should be zero.

Sensitivity can be expressed as the ratio of faradaic current to non-faradaic current and the non-faradaic current is inversely proportional to the size of electrode. The peak current (faradaic current) is expressed by:

$$i_{max} = 2.59 \times 10^5 n^{\frac{3}{2}} (Dv)^{1/2} C_v \quad (5)$$

where v is the constant rate of variation and C_v is the values of ionic activity. And, non-faradaic current is expressed by:

$$i_{ch} = C\frac{dE}{dt} = \pm Cv \quad (6)$$

From (5) faradaic current is proportional to the square root of scan rate v and non-faradaic current is proportional to the scan rate as shown in (6). Hence, the ratio

Imax /I_{ch} is inversely proportional to scan rate. Thus increasing scan rate will reduce measuring sensitivity. Thereby, relatively low scan rates are preferred in measurements at solid electrode [18].

2.3 Electrochemical Sensors

The principle of all electrochemical sensors is to measure certain variables of an electrochemical cell by observing the change in current, potential, or concentration. Electrochemical sensors are broadly classified into three categories [19]:

2.3.1 Voltammetric sensors

In voltammetric sensors, the voltage is applied across the electrodes of the electro-chemical cell and the current flowing between them is measured. The measured current is due to the response of chemical species of interest. Voltammetry improves the sensitivity by increasing the ratio of the faradaic current (the current of interest) and non-faradaic current (the background). By applying linear, square or cyclic voltammetry, improved selectivity and sensitivity is achieved.

A periodic triangular voltage waveform is applied between the working and the reference electrodes and the current response of the cell is monitored. The waveform is linearly scanned in a potential window with a lower or initial value of V_i and the upper or final value of V_f, at a given scan rate of v.The subsequent plot that is obtained is called cyclic voltammogram. Cyclic voltammetry is commonly used for microelectrode (i.e., electrodes with dimensions on the order of micrometers) to reduce the non-faradaic current.

In chronoamperometry electrochemical analytical technique, the potential of the working electrode is stepped, and the resulting faradaic current (caused by the stepped potential) is measured as a function of time [16].

AC voltammetry has been shown to have better sensitivity compared to cyclic voltammetry. Low amplitude AC potential signals above the linear scan are applied as stimulus and the AC components of the redox current generated are measured. Thus in case of sinusoidal stimulus, AC non-faradaic current has a phase lead of 90^0 and the AC faradaic current has phase lead of 45^0 or less depending on the type of reactant being examined with respect to the applied AC voltage. The sensitivity is about 10^7 times better than cyclic voltammetry [20].

2.3.2 Amperometric Sensors

Amperometry is a special type of voltammetry, where the voltage applied across the electrodes of the electrochemical cell is kept constant while its current is measured. The measured current is a function of the concentration of the electroactive species. The response will have high linearity if the current is limited by the rate of the mass transfer and not by the rate of charge transfer [16].

2.3.3 Potentiometric sensors

Potentiometric sensors, in which the open circuit electrochemical cell potential is measured, which according to the Nernst equation 2.3 is proportional to the logarithm of the concentration of the chemical species of interest. Potentiometric sensors are commonly used when the concentration of chemical specie to be measured changes over several orders of magnitude (e.g., in the case of pH measurements). In cases, where the concentration changes over only one or two orders of magnitude (e.g., in the case of glucose concentration in physiological fluids), a sensor with a linear relationship between response and concentration is preferable (such as Amperometric sensors) rather than logarithmic response [21].

2.3.4 Conductometric sensors

Conductometric sensors, in which the conductance of the electrochemical cell is measured by an alternating current bridge method. In this kind of sensor mostly the resistive component of the impedance of the chemical specie is measured. The measurement is performed at one fixed frequency [22].

Biosensors

A biosensor is made of biological materials, e.g., tissue, micro-organisms, enzymes, antibodies, nucleic acids and so on, to detect chemical species such as glucose, urea, lactate, etc. [19]. the ability of biosensors to be sensitive and selective to a particular type of biological material makes it attractive. A biosensor comprises of two parts:

- A biological element such as enzymes or antibodies or micro-organisms.
- An optical or an electrochemical detector.

The selectivity of a biosensor is limited by the biological element, whereas the sensitivity depends on both biological element and the transducer (optical or electro-chemical). The property of selecting a particular biological material gives biosensor edge over chemical sensors.

2.4 Electrochemical Glucose Biosensors

Electrochemical detection of glucose concentration is based on the use of glucose oxidase. In normal conditions, glucose oxidase enzyme oxidizes with the glucose to form gluconic acid, changes into an inactivated reduced state by accepting electrons. This reduced enzyme returns to active oxidized state by giving these electrons to molecular oxygen and thereby producing hydrogen peroxide (H_2O_2). This process is illustrated in Figure 2.3 and is represented by the reaction:

$$Glucose + O_2 \xrightarrow{GOx} Gluconice\ Acid + H_2O_2 \quad (7)$$

The glucose oxidase (GOx) enzyme acts as a catalyzer for the oxidation of glucose and is not consumed in the reaction. From the above reaction, there are few possibilities for detecting the glucose concentration [21]. The first method is to use an amperometric sensor to measure the amount of oxygen consumed or to measure the hydrogen peroxide produced in the reaction. Second method is to use a potentiometric sensor to detect the change in pH level caused by the production of gluconic acid. Third method is to use a conductometric sensor to detect the change in electrical resistance due to the reaction.

Potentiometric and conductometric glucose biosensors, are sensitive to the interfering biological species other than glucose and, also the response of potentiometric sensors demonstrate a logarithmic response to detect glucose concentration, which further limits the potentiometric sensors sensitivity [21]. Amperometric glucose biosensors are widely used to detect glucose concentration as they generate electric current which is linearly proportion to the glucose concentration being sensed.

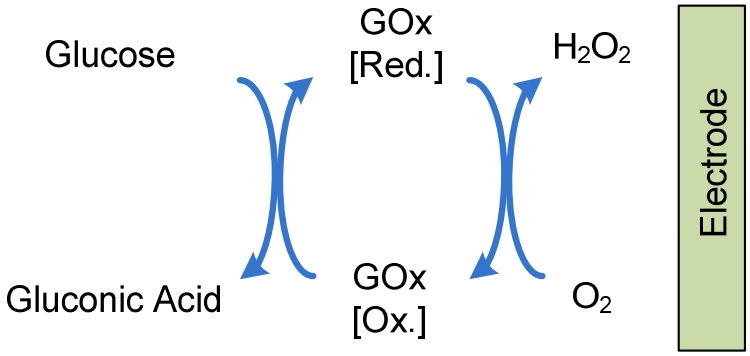

Figure 2.3 Enzymatic reactions between glucose and glucose oxidase.

2.4.1 Amperometric glucose biosensors

Amperometric glucose biosensors are broadly classified into three generations [21]. In the first generation sensors, the hydrogen peroxide produced or the oxygen consumed in the reaction 2.6 is detected. In the second generation, a mediator is used to transfer electrons from the reduced enzyme to the electrode. The third generation of amperometric biosensor is based on direct electron transfer between the enzyme and electrode.

First Generation of Electrochemical Glucose Biosensors

The first generation glucose sensors are separated into two categories: hydrogen peroxide electrode-based (H_2O_2) biosensors and oxygen electrode-based (O_2) biosensors.

The H_2O_2-based sensors measure hydrogen peroxide produced in the enzymatic glucose reaction. These sensors are easy to fabricate and screen printing is used to miniaturize them. However, these sensors have a few drawbacks.

1. Enzymatic reaction is oxygen limited.
2. Hydrogen peroxide produced by the reaction over a period of time inactivates the glucose oxidase.
3. High operating voltage required for oxidizing the hydrogen peroxide may also trigger the interferers such as urea and acerbate (vitamin-C).

In O_2 based biosensors, oxygen consumed in the enzymatic reaction is measured. This method is not restricted by oxygen deficit and interference problems. Nevertheless it still has short life time problem due to production of hydrogen peroxide. The other drawbacks are slow response time, requirement for more complex electronic circuitry, difficulties in miniaturization, and low accuracy and reproducibility [21].

Second Generation of Electrochemical Glucose Biosensors

In the second generation glucose biosensors, a mediator (chemical component) is added to transfer the electrons from the reduced enzyme to the electrode Figure 2.4. The oxidation potential of the mediator could be much lower than that of hydrogen peroxide, thereby minimizing the interference problem. Also, the signal generation is independent of oxygen. Thus this method is widely used to detect, the true glucose concentration in the subcutaneous tissue.

The drawbacks associated with these sensors is that, mediator could leak out of the electrode surface, and secondly most of the proposed mediators are toxic, which makes their implantation hazardous [21].

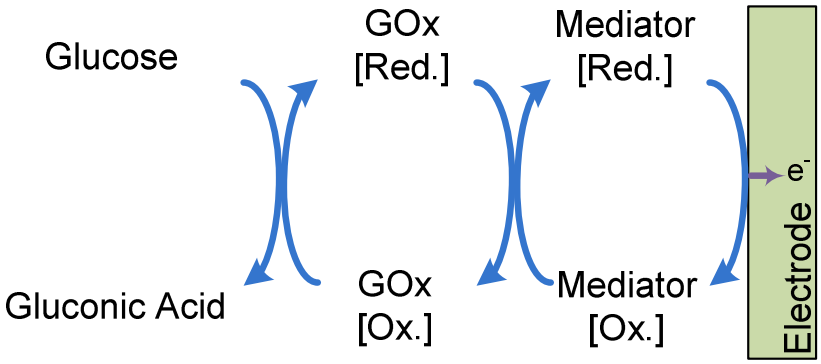

Figure 2.4 Glucose measurement with second generation glucose sensor.

Third Generation of Electrochemical Glucose Biosensors

The third generation glucose biosensor is based on the direct electron transfer between the enzyme and the electrode without any mediator [23]. With new electrode materials such as organic conducting salt and organic conducting substances, the direct electron transfer from enzyme to the electrode is achieved.

These biosensors have low operating potential, and thereby will overcome the interference problem. Since there is no soluble or partially soluble compound involved in

the construction of this sensor, it is most suited for implantable electrochemical biosensors.

2.4.2 Enzymatic and Non-enzymatic glucose sensors

Enzymatic glucose sensors

The basic concept of an enzymatic reaction is that the biological recognition entity reacts with the enzyme and in turn, is transformed into reaction products as shown earlier in (7). GOx is the standard enzyme in enzyme-based glucose sensor due to a high selectivity for glucose, ease of obtainment, cheap, ionic strength, and its relative temperature stability. The mechanism of a GOx based glucose sensor is based on immobilized GOx catalyzing the oxidation of glucose by molecular oxygen, and then glucose is oxidized to gluconic acid and hydrogen peroxide. Majority of the commercially available glucose sensors are enzyme based. Common drawbacks of enzymatic glucose sensors are insufficient sensor data stability, complexity of the enzyme immobilization, and oxygen [24]. Sensors based on GOx that are exposed to heat or unwanted chemicals, GOx may lose its activity quickly. In addition, the performance of GO_x based glucose biosensor is limited by the electron transfer between the enzyme and the electrode because the catalytically active centers of GO_x are covered by the protein shell, therefore the direct electron transfer from the enzyme to the electrode is difficult [25]. Another issue of the enzymatic glucose sensor is the immobilization of the enzyme on the electrode.

Non-enzymatic glucose sensors

Direct glucose oxidation at a noble metal electrode which has a large surface area shows considerable signal to noise ratio allowing for the measurement of glucose in blood without the use of an enzyme [26]. The electrocatalytic principle of non-enzymatic sensors has long-term stability and reproducibility free from oxygen dependency, enzyme

immobilization, and the intrinsic instability of enzymes. The mechanism of direct electrochemical oxidation of glucose may be applied to other non-physiological areas such as the food industry, industrial process, the development of fuel cells, and batteries. Non-enzymatic electrocatalysts consist of various forms, such as metals (e.g., Pt, Au), metal oxide (e.g., MnO_2, RuO_2), alloys (e.g., PtPb, PtRu), complexes (e.g., cobalt phthalocyanine), and carbon materials (e.g., carbon nanotubes, boron doped diamond).

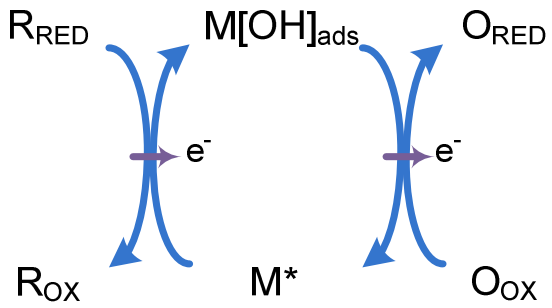

Figure 2.5 Non-enzymatic reaction mechanism.

Figure 2.5 shows more how the oxidation and reduction processes are catalyzed at the metal surface. M* is the reductive metal adsorption site and $M[OH]_{ads}$ is the oxidative adsorbed hydroxide radical. The faradaic currents of glucose associated with kinetically controlled electrochemical events which are proportional to the nanoscopic surface area of the electrode, rather than its macroscopic flat area. Therefore, a deeper and denser electrode, which has larger nanoscopic surface area, enhances the faradaic currents. The electron transfer rate of the interference species, like ascorbic acid (AA) and acetaminophen (AP), is faster than that of glucose. As a result, the faradaic currents of rapidly oxidizable / reducible reactants such as AA and AP are sensitive only to the surface area of the electrode which results in the reduction of the electrochemical events.

Non-enzymatic glucose sensor design provides an alternative method, but sensitivity has not been sufficient enough for practical applications. With advancements in nanotechnology, the sensitivity of non-enzymatic glucose sensors based on direct oxidation on the nanoporous electrode has risen considerably and gives physiologically useful sensitivity [27]. Nano-scale electrodes make a very high electro-active surface area that is considerably larger than the geometric surface area, resulting in enhancement of electro-catalysis [28].

2.5 Three-Electrode Measurement System

All electrochemical cells require at least two electrodes immersed in an electrolyte and the potential of a given electrode will be measured relative to another electrode (the reference electrode). Potentiometric measurements require two electrodes, because no currents flows through the cell, there is no voltage drop across the solution resistance and the potential of reference electrode remains constant.

Voltammetry measurements need an external precise potential applied to the electrochemical cell, and the current that flows through the cell is measured. But it is not generally possible to provide accurately controlled cell potential in a two electrode system, as there would be potential drop due to the cell current flowing through the finite solution resistance. Also, the cell current flowing through the reference electrode will slightly polarize it, meaning its interfacial potential difference changes to some extent. Moreover, reference electrode material reduces due to the current flow is another problem of two-electrode systems [29]. This problem can be reduced by using a very large reference electrode and a very small working electrode. However, using a large reference electrode is not feasible when the goal is to miniaturize the electrochemical cell.

In a three electrode system, as shown in Figure 2.6, better potential control is attained by adding a new electrode (counter electrode) into the electrochemical cell. The potential of the working electrode is controlled relative to the reference electrode, and the current is sourced into the solution by a third electrode called the auxiliary or counter electrode (CE) [16]. The current of the cell can be measured either at the working electrode or at the counter electrode.

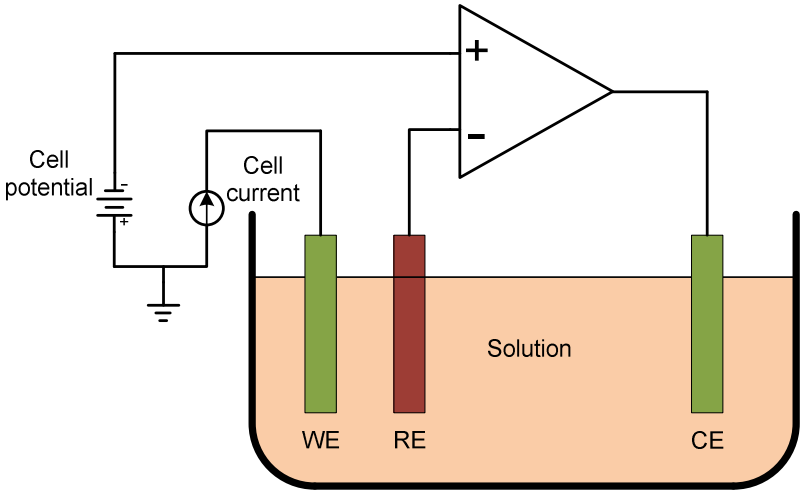

Figure 2.6 Three-electrode electrochemical cell.

The stimulus for a three electrode system is applied by using an electronic instrument, called potentiostat. It accurately controls the potential difference across the working electrode and the reference electrode, using a negative feedback loop which injects the proper amount of redox current into the counter electrode to keep the potential difference between the working and reference electrodes at a desired electrochemical cell potential [16].

2.5.1Sensor electrode circuit model

For proper design a potentiostat and readout circuit through simulation, an electrical equivalent model of the electrochemical cell is required. For an ideal polarizable

electrode, the impedance of the electrode consists of the double layer capacitance, C_{dl}, in parallel with R_{ct} in series with the solution resistance, R_S.

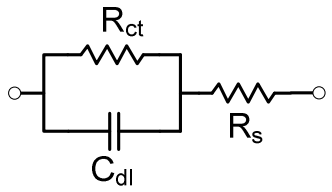

Figure 2.7 Equivalent circuit model of an electrode

Double-layer capacitance is very difficult to model as it is a nonlinear capacitance whose value depends on many parameters such as applied potential across it, temperature, ionic concentrations, types of ions, oxide layers, electrode roughness, impurity adsorption and so on. However, using a simple modeling approach, C_{dl} can be approximated by:

$$C_{dl} = K_{dl}A \tag{8}$$

where A denotes the area of the electrode, and K_{dl} is a constant typically in the range of 10-100μF/cm^2.

Solution resistance usually has a great effect on the impedance of an electrochemical cell. The resistance of an ionic solution depends on the ionic concentration, type of ions, temperature and the geometry of the area in which current is carried [30]. Assuming a uniform current is flowing though a bounded volume of the solution with an area of A and a length of l, the resistance can be calculated by:

$$R_s = \rho \frac{1}{A} \tag{9}$$

where ρ is the solution resistivity.

For a real electrode, when the electrode/solution potential is forced away from its open-circuit potential, an electric current flows through the electrode surface whose value

is controlled by the kinetics of the reactions taking place at the electrode surface and by the rate of mass transfer of the reactants towards and away from the electrode surface. R_{ct} is a resistance which represents charge transfer at the electrode surface.

$$R_{ct} = \frac{RT}{nFi_o} \quad (10)$$

where i_o is the exchange current density, n is the number of electrons transferred, R is the molar gas constant, T is temperature, F is Faraday's constant.

The impedance of an electrochemical cell is usually experimentally measured over a wide frequency range (usually from 1 mHz to 20 kHz) and then, using a non-linear least squares fitting program, an equivalent circuit is fitted to the experimental data. In Electrochemical Impedance Spectroscopy (EIS), the impedance of an electrochemical cell is measured over a frequency range. This is a powerful tool for the analysis of complex electrochemical systems and to experimentally model the electrical equivalent circuit of the electrochemical cell (working, reference, counter electrodes and solution resistances) [31].

The electrical equivalent circuit model of the three-electrode glucose sensor is shown in Figure 2.6. C_{ce} and C_{we} is the double layer capacitances of CE and WE. R_{CE}, R_{RE} and R_{WE} represent the charge transfer resistances of the CE, RE, and WE. R_{s1} and R_{s2} represent the solution resistance [22].

Table 1 Sensor model components description

Component	Description
C_{ce}, C_{we}	Double layer capacitances
R_{ce}, R_{re}, R_{we}	Charge transfer resistances
R_{s1}, R_{s2}	Solution resistances

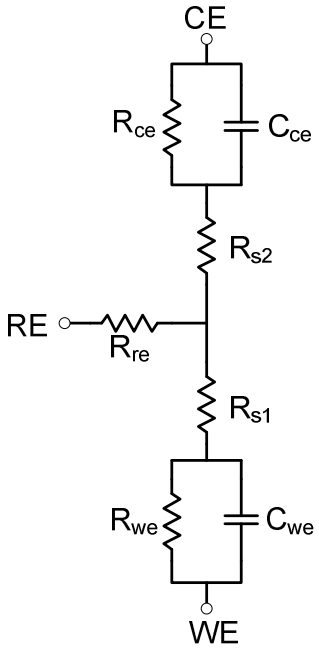

Figure 2.8 Three electrode electrochemical sensor model.

2.5.2 CMOS Readout Circuits

Transimpedance amplifier with a resistive feedback Figure 2.9 is the most widely used method for current measurement by converting input current I_{IN} to output voltage $V_O = -I_{IN}R_F$ where R_F is the transimpedance amplifier feedback or gain resistance .

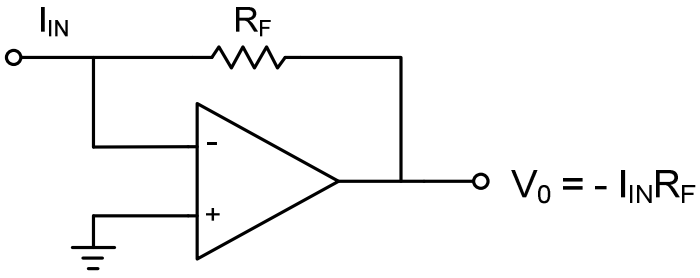

Figure 2.9 Current measurement using a transimpedance amplifier.

The high gain operational amplifier (op-amp) forces a virtual ground at the working or counter electrode to allow the cell current to flow through the op-amp via feed-back resistance RF, hence generates an output voltage linearly proportional to IIN. This method has a few drawbacks.

- The feedback resistor along with the capacitance of input device creates a pole at the input, degrading the stability and pulse response [32].
- Large value of feedback resistance is required to measure smaller input currents and very large resistors are difficult to realize in integrated circuit design [33].
- The feedback resistance generates thermal noise $4kTR_F$ where k is Boltzmann constant 1.38 x 10-23 J/K and T is 290K). This is an additional component in the output noise of trans-impedance amplifier [34].

Another approach for the current measurement is to place a resistor in the current path of working electrode and measure the voltage built across that resistor [33] and the voltage can also be amplified before measurement and are implemented as shown in Figure 2.10.

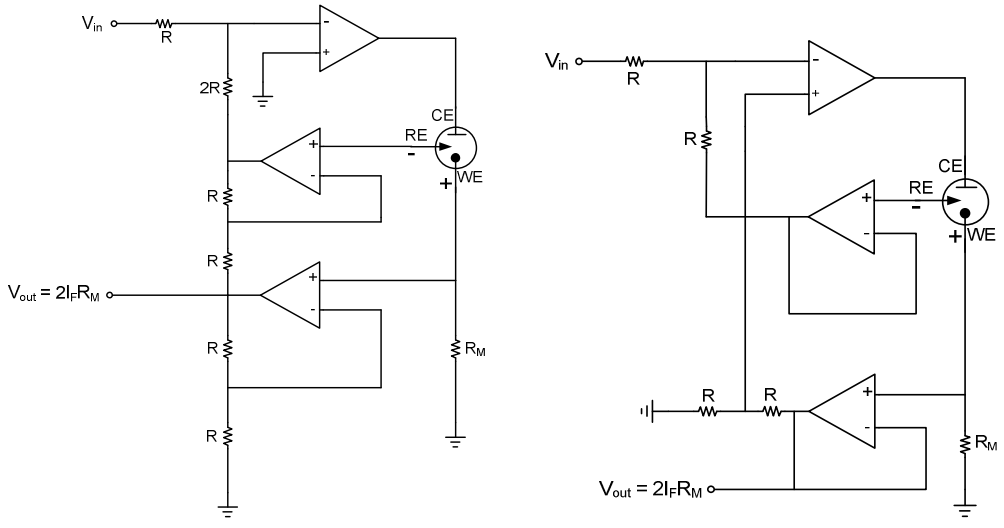

Figure 2.10 Readout circuits (a) and (b) show current measurement by placing resistor in current path.

The potential across the working electrode changes depending onI_{IN}. Thus, for proper potential control, the measured potential is fed-back to control amplifier [33]. This method is complex and noisier compared to a transimpedance amplifier. It is also more prone to mismatch between components, as it requires more active and passive components.

The third method for current measurement is to place a resistor in the current path of the counter electrode, as shown in Figure 2.11 and an instrumentation amplifier is used to measure the voltage across the resistor [35]. This method needs more components than the previous two methods, thereby causing greater mismatch between components and generates high noise. In this method both measured voltage and current are referenced to ground [33].

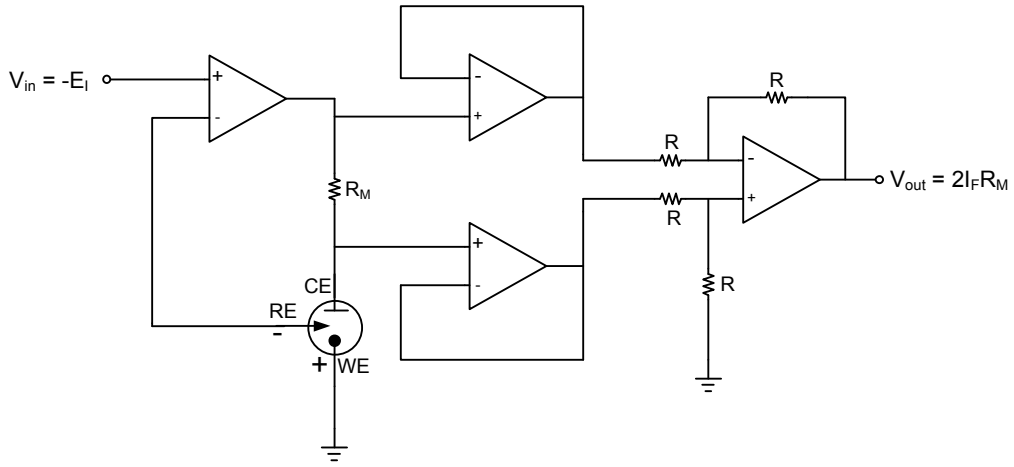

Figure 2.11 Instrumentation amplifier.

Another approach is to use switch capacitor circuits like the one in Figure 2.12. When the clock signal is low, sensor current charges an integration capacitor to the output voltage. When the clock signal goes high, the capacitor is discharged. The circuit

functions similar to transimpedance amplifier with a feedback resistor. The gain of the switched capacitor circuit amplifier is controlled by the pulse width of the switch timing signal.

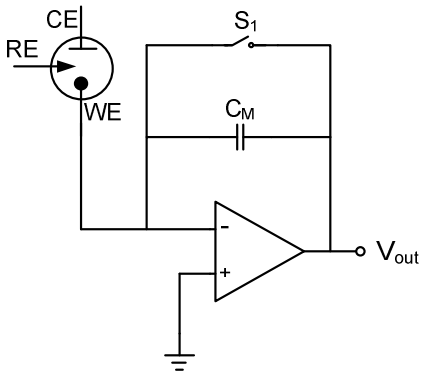

Figure 2.12 Switched capacitor transimpedance amplifier

The switched capacitor transimpedance amplifier does not have the thermal noise contributed by the feedback resistance in conventional transimpedance amplifiers. The disadvantage is that it includes the switching noise caused by the switch which can leak and add to capacitor voltage. Another problem is that switched capacitor circuits are more complex than the simple one shown in Figure 2.12 and involve several switches with different clock phases [36][37]. This requires good phase locking between the various clocks used for switching which extends the complexity of the system. This also adds a lot of substrate noise from digital switching which could affect the linearity of the output.

Chapter 3

Microneedle Based Non-Enzymatic Painless Glucose Sensor

Microneedles are small mechanical structures that interface between a micro-system and an organism such as the human body. Figure 3.1 shows a schematic cross-section of the human skin. The epidermis is typically 100 µm thick and forms the outermost layer of the skin. Only very few nerve endings are located in the epidermis so that only little or no sensation of pain may be associated with epidermal insertion of microneedles. The stratum corneum is the outermost layer of the epidermis and protects the body from the environment. The stratum corneum essentially consists of flat dead skin cells that are tightly packed together and is approximately 20 µm thick, however, it also forms the calices that can be substantially thicker, for example on the palms of the hands. The dermis is located underneath the epidermis and contains the nerve endings as well as blood vessels. The thickness of the dermis varies between 0.6 mm and 3 mm. The subcutaneous fat layer is situated underneath the dermis. The interstitial fluid of the epidermis also contains many molecules of biological interest such as glucose. Microneedles therefore offer minimally invasive access to a site for sensing of these compounds in the body [33].

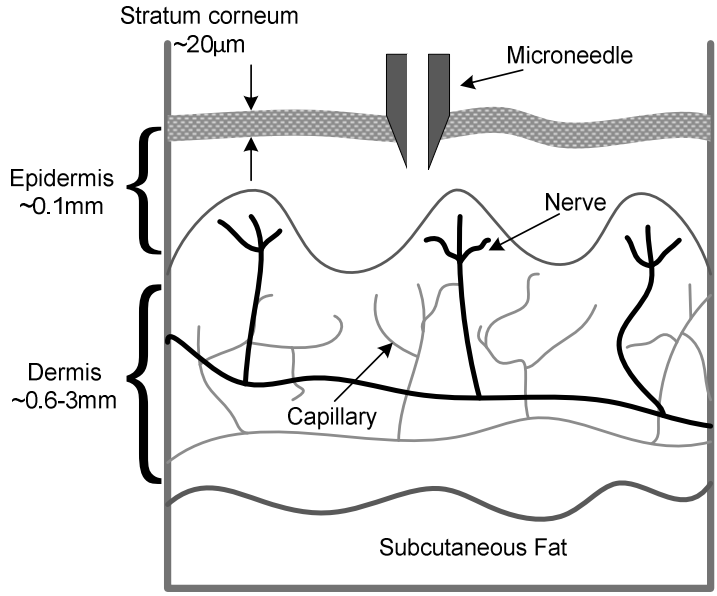

Figure 3.1 Structure of Skin

Since the skin consists of a very flexible tissue with the stratum corneum as the protective layer has several implications for the mechanics of penetration of the stratum corneum by microneedles. The needle shaft might need to be longer than the intended penetration depth because of skin deformation during insertion. A needle array that is too dense will rather press the skin uniformly down instead of penetrating the stratum corneum.

Microneedles are still the ideal instrument to behave miniaturized hypodermic syringes which are long enough to penetrate the stratum corneum but short enough not to penetrate deep into the subcutaneous layer. Such injections avoid contact with the blood vessels of the dermis, and reduce the risk of infections. This allows minimizing the stimulation of the nerve endings located deeper in the skin making it minimally invasive and relatively painless [38].

The most common application for microneedles is injection or sampling of compounds. Out-of-plane microneedle designs allow high-density arrays where the

needles or probes can be packed closely together and interfaced with a wide area. Microneedles are fabricated using micro-electromechanical system (MEMS) technology, which has been derived from integrated circuit (IC) fabrication technology. MEMS fabrication features special processes that allow forming mechanical structures, while pattern transfer is commonly based on photolithography methods.

Another advantage of microneedle is monolithic integration with CMOS. Bringing the CMOS readout circuit closer to the detection site will reduce the noise and therefore increase the signal-to-noise ratio. This might then allow reducing the sample volume, and hence the required number of needles. The combination of microneedles and CMOS will enable development of compact and low cost glucose sensing products [33].

Yoon et.al [12] has developed a microneedle based painless non-enzymatic glucose sensor. Since diabetes mellitus is a disorder of the metabolism that requires constant monitoring of blood glucose concentrations, diabetic individuals with trypanophobia (the fear of needles) may especially benefit from this new technology. To achieve this goal, a 15 × 15 microneedle array was integrated into our device to provide a painless measurement option to diabetic patients, instead of the traditional “fingerprick” method. A non-enzymatic painless glucose sensor is designed, fabricated, and characterized for diabetes testing applications.

Carbon nanotubes (CNTs) have an intrinsically high active surface area that is ideal for a kinetically controlled, surface bound reaction like direct glucose oxidation. Active surface area of platinum nanoparticles coated CNT was shown to be up to 150 times greater than the surface area of a similar planar platinum electrode. A sharp silicon microneedle array (380 μm tall, 1 μm tip diameter) was formed by unique combination of dry and wet etching. To substantially increase the surface area multi-walled carbon nanotubes (MWCNTs) were grown directly on non-planar sharp silicon microneedle

array. It was followed by platinum (Pt) nanoparticle (NP) catalyst decoration on the MWCNT forest by electroplating. Therefore, platinum decorated multi-wall carbon nanotubes were used for the electrocatalytic glucose sensor in an *in-vitro* experiment, and showed reasonable sensitivity in the range of 8.10 ~ 13.67 μA/mM-cm2 under physiological level of 0 ~ 15 mM glucose. Figure 3.2 shows a close-up view of the micro-needle with 380um height [38]. Figure 3.3 shows a 3D structure of the final fabrication sequence of the complete sensor [38]. The figure shows two symmetrical electrodes.

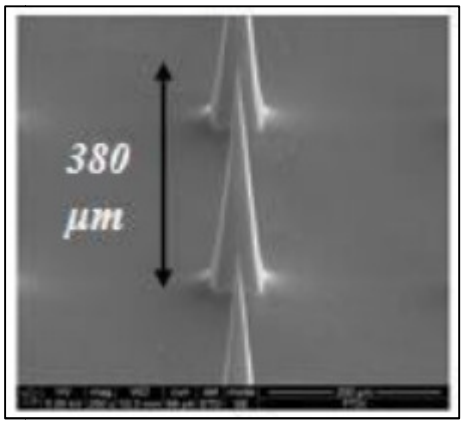

Figure 3.2 SEM image of the microneedle [38]

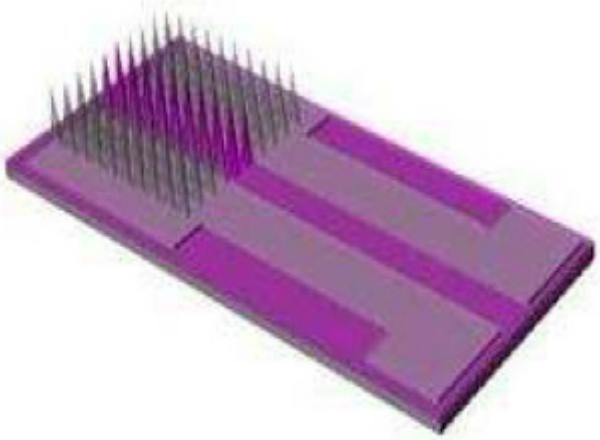

Figure 3.3 Microneedle-integrated non-enzymatic glucose sensor structure [38]

However, for practical use, selectivity experiments must be performed in the presence of interfering species such as ascorbic acid, acetaminophen, etc. to increase reliability. Additionally, the reference electrode integrated into the sensor device. Since the glucose sensor is microneedle-based, this will enable “painless” glucose sensing.

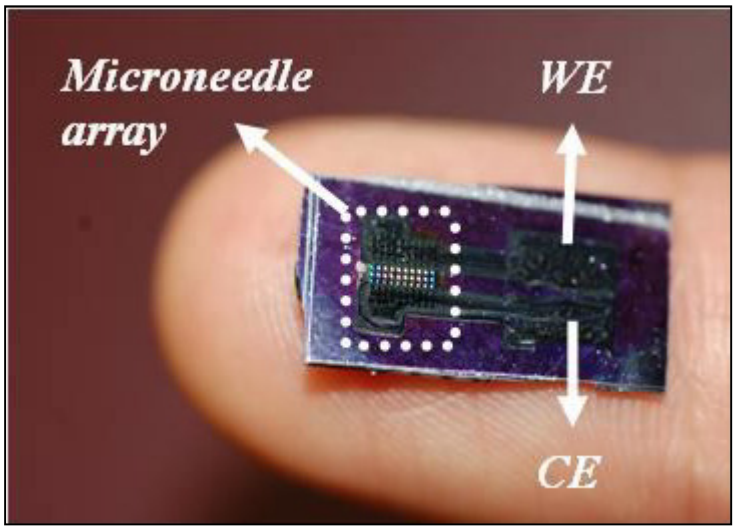

Figure 3.4 Microneedle-integrated non-enzymatic glucose sensor photo [38]

To develop a commercially feasible glucose sensor, a miniaturized silver/silver chloride electrode integrated 3-electrode glucose sensor was developed and *in-vitro* performances were investigated. Figure 3.4 shows an image of the fabricated microneedle-integrated non-enzymatic glucose sensor. The sensitivity of the newly designed painless non-enzymatic 3-electrode glucose sensor was increased as high as 17.73 ± 3 μ A/mM-cm^2 and showed excellent selectivity over typical interference agents such as acetaminophen and ascorbic acid [38].

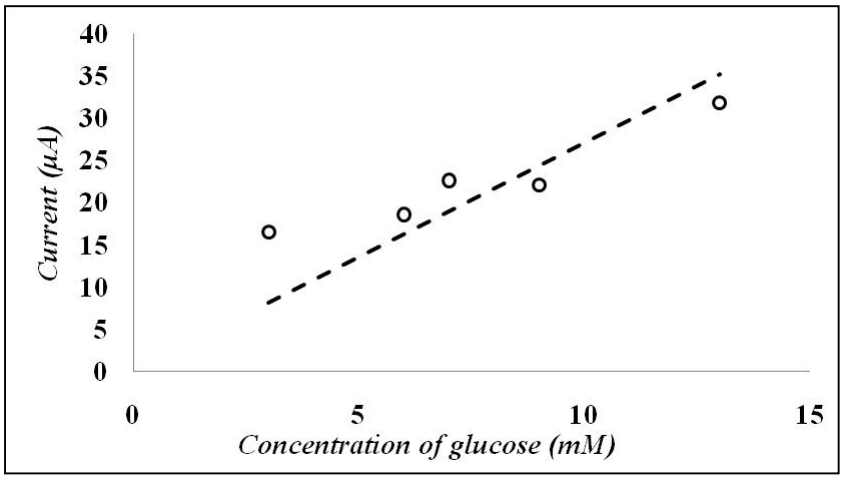

Figure 3.5 Glucose sensor response [12].

The current response Figure 3.5 of the microneedle based non-enzymatic glucose sensor is obtained for various glucose concentrations in the range of 3mM - 13mM in 0.1M phosphate-buffered saline (PBS). The amperometric current response was linearly decreased in the presence of interfering species such as relevant physiological levels of acetaminophen (AP), and ascorbic acid (AA) at potential of + 0.4 V (vs. Ag/AgCl) in 0.01M, pH 7.4 PBS solution. This new sensor may provide a painless blood glucose testing option for those who suffer from hyperglycemia (high blood sugar).

Chapter 4

CMOS Analog Correlator Based Glucose Sensor Readout Circuit

The analog correlator based glucose sensor readout circuit offers lower noise and wider dynamic range compared to the conventional TIA architecture. This chapter introduces matched filter theory and its practical implementation and analysis. This is followed by a PCB implementation of the proposed circuit. Then the design analysis of these two core circuits and the overall system in CMOS is discussed. The simulation and measurement results of the IC are shown at the end of the chapter.

4.1 Design of Proposed Glucose Sensing Readout Circuit

In wireless receivers, the method extraction of the baseband signal from the modulated waveform has a great impact in the performance of the system particularly the signal-to-noise ratio (SNR). In typical communication systems it is required to detect the signal in noisy environment while in case of digital communication systems decision has to be made from received signal if logic 0 or logic 1 is transmitted. Thus the appropriate figure of merit in case of digital systems is probability of error. In case of radars it's not only the decision making about logic 0 or logic 1 but we also need to extract the information about target like the distance, velocity etc.

Let's consider the received signal is r (t). This signal might be a combination of both noise signal n(t) of power density $N_0/2$ watts and signal s(t) which received from the transmitter. If the signal of logic 0 is received from the transmitter then r(t) will only contain noise signal n(t). To achieve optimum detection we have to operate on r(t) and it is required to find out if the received signal contains information signal s(t) or not. This looks like a filtering function where it is required to filter out information signal from the noise signal. Let's consider linear filter to do this job.

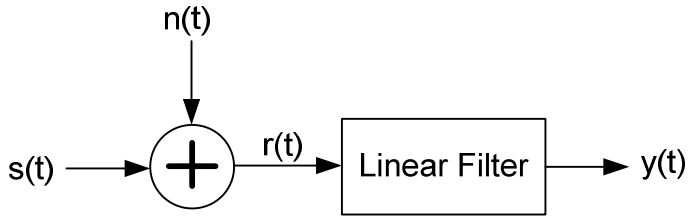

As the filter is assumed to be linear its output y(t) can be represented as follows

$$y(t) = y_s(t) + y_n(t) \tag{11}$$

Where $y_s(t)$ is filter out put due to signal and $y_n(t)$ is the filter output due to noise signal. Whenever information signal s(t) is present in r(t) it is required for the filter to increase the instantaneous power of the $y_s(t)$ compared to $y_n(t)$. Thus it is required for the filter to have maximum signal to noise ratio (SNR).

One solution to the problem of optimum detection is to use matched filters. If s(t) is any waveform, then a filter which is matched to the s(t) is by definition, one with the impulse response

$$h(t) = s(t_m - t) \tag{12}$$

Where t_m is an arbitrary constant. Matched filter is a circuit (Figure 4.2) with an impulse response $h(t)$ which is a conjugate of the input signal $s(t)$reversed in time and shifted to the right by the sampling bit period as seen in Figure 4.1.

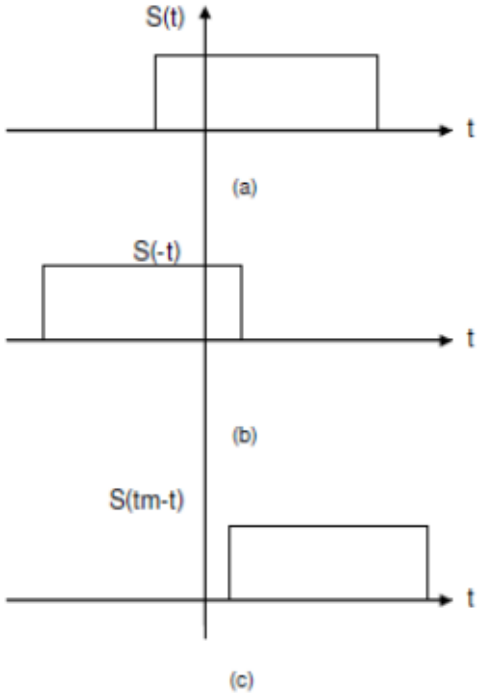

Figure 4.1 (a) shows the signal waveform (b) shows reversed signal in time domain s(-t) and (c) shows signal shifted by constant tm, s(t_m-t)

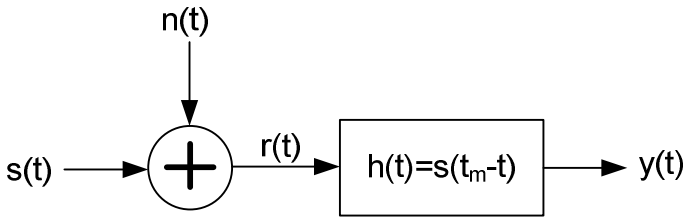

Figure 4.2 Matched Filter

Here $n(t)$ is the additive white noise added from the channel. The output of the filter achieves maximum SNR which only depends on the energy of the input signal and not its shape or bandwidth. It can be mathematically proven that the matched filter is equal to applying the correlation function on the input signal.

Mathematical Derivation of match filter

Let's assume that signal $r(t)$ received at instants $T = t_0$ contains information signal $S(t)$. Thus it is necessary for the filter to give maximum SNR at T = t_0. Let's assume that transfer function of the filter is $G(j2\pi f)$, then the output noise power density at the output of the filter is given by

$$\frac{N_o}{2}\int_{-\infty}^{\infty}|G(j2\pi f)|^2 df \tag{13}$$

Also if $s(t)$ is the signal then $S(j2\pi f)$ is the spectrum of the signal. Then output of the filter is given by $S(\,j2\pi f\,) * G(\,j2\pi f\,)$ and out of the filter at $T = t_0$can be found out by inverse Fourier transform

$$y_n(t_0) = \int_{-\infty}^{\infty} S(\,j2\pi f\,)\,G(\,j2\pi f\,)e^{j2\pi f t_0} df \tag{14}$$

The signal to noise ratio is given by the ratio of the square of (14) and (13). It is required to have maximum value of this ratio.

$$\rho = \frac{2\left[\int_{-\infty}^{\infty} S(\,j2\pi f\,)\,G(\,j2\pi f\,)e^{j2\pi f t_0} df\right]^2}{N_0\int_{-\infty}^{\infty}|G(j2\pi f)|^2 df} \tag{15}$$

It can be seen that numerator of the (15) is real. And identifying $G\,(j2\pi f)$ as $f(x)$ and $S(\,j2\pi f\,)e^{j2\pi f t_0}$ as $g(x)$ Schwarz inequality gives

$$\left|\int f(x)g(x)dx\right|^2 \le \int|f(x)|^2 dx \int|g(x)|^2\,dx \tag{16}$$

If $f\,(x) = K * g(x)$ hence

$$G(\,j2\pi f\,) = K\,S(\,j2\pi f\,)e^{-j2\pi f t_0} \tag{17}$$

Thus by using expression (17) one can obtain

$$\rho \le \frac{2}{N_0}\int_{-\infty}^{\infty}|S(j2\pi f)|^2 df \tag{18}$$

As $|S(\,j2\pi f\,)|^2$ is the energy of the signal (18) can be written as

$$\rho \leq \frac{2E}{N_0} \tag{19}$$

Thus filter with transfer function $G(j2\pi f) = KS(j2\pi f)e^{-j2\pi f t_0}$ maximizes the SNR at T = t_0. Let signal received is given by

$$r(t) = s(t) + n(t) \tag{20}$$

Filter impulse response is given by

$$h(t) = S(t_0 - t) = p(t_0 - t) \tag{21}$$

output of the filter is the convolution of $r(t)$ and $h(t)$

$$y(t) = \int_{\infty}^{\infty} r(t)h(t-x)dx \tag{22}$$

where $h(t) = p[t_0 - (t-x)] = p(x + t_0 - t)$ thus substituting $h(t)$ as $p(x + t_0 - t)$

$$y(t) = \int r(x)\, p(x - t_0 - t)dx \tag{23}$$

at $t = t_0$

$$y(t_0) = \int_{0}^{t_0} r(x)p(x) \tag{24}$$

The correlation function in (24) can be implemented as a practical circuit shown in Figure 4.3. It consists of a multiplier and an integrator both of which can be realized using analog CMOS circuits.

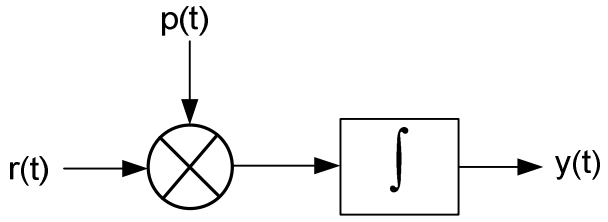

Figure 4.3 Optimum detection using a Correlator

Figure 4.4 illustrates how the correlator circuit works. Here the input signal is assumed as a sine wave and is added to white gaussian noise. The noise corrupted sine wave is multiplied to a template sine wave of a similar shape (same time period and phase) which is then integrated. The peak of integrator's output is sampled to extract the signal. Since the input noise is not of the same shape as the template, the corresponding multiplier and integrator output is small hence rejecting the noise. Meanwhile the signal having the same shape as the template gives a large output, hence maximizing the SNR.

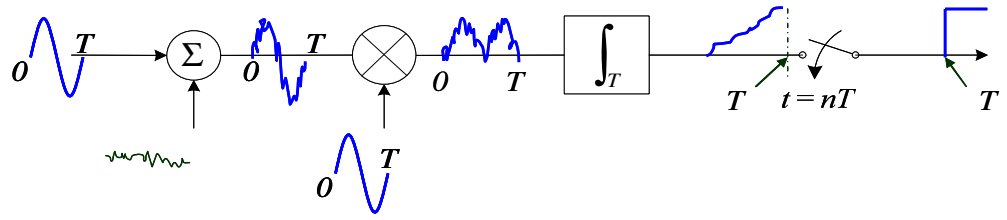

Figure 4.4 Operation of the correlator circuit

The correlator circuit will achieve maximum SNR if the input signal $x(t)$ and the template signal $p(t)$ have the same shape and are synchronized. Timing misalignment results in a lower SNR at the correlator output. The correlator circuit is used for coherent detection in wireless receivers for communication and radar but can be extended to other systems.

This work proposes an analog correlator based readout circuit for glucose sensing shown in Figure 4.5. A glucose sensing system requires having low noise and high linearity. This gives it a wide input dynamic range to measure the full range of glucose level in blood, tear or other media. An analog correlator based readout circuit can achieve better noise and linearity performance as compared to conventional current-to-voltage conversion circuits.

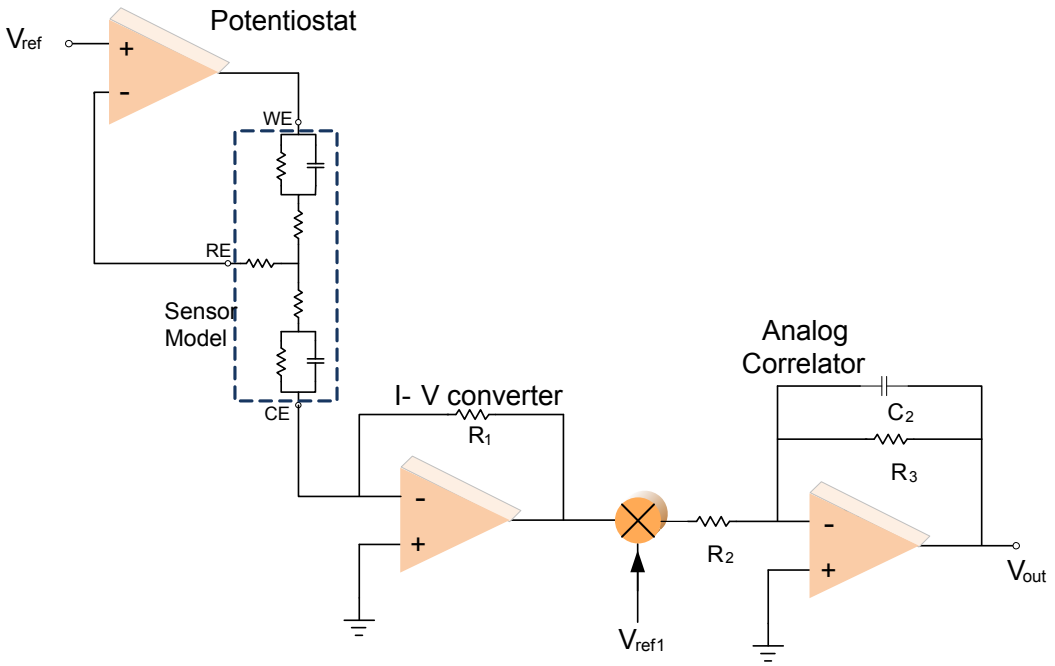

Figure 4.5 Proposed glucose sensor readout system.

Figure 4.5 shows a typical potentiostat and I-V converter circuit around a 3 electrode sensor represented by a sensor model. This part of the circuit is common to all trans-impedance amplifier systems. The I-V converter is followed by the analog correlator which comprises of a multiplier and an integrator realized using an op-amp. Since the input signal in a glucose sensing system is a DC signal and the template signal required for the multiplier input should be of the same shape, a reference voltage V_{ref1} is provided for the second multiplier input. The integrator is a typical inverting op-amp configuration with a capacitive feedback C_2 and resistance R_2 between the multiplier output and the negative input of the op-amp. A feedback resistor R_3 in parallel with capacitor C_2 is also provided to define the DC voltage at integrator's output node and prevent it from floating.

$$A_{\text{int}} = -\frac{R_3}{R_2}\left(\frac{1}{sR_3C_2 + 1}\right) \tag{25}$$

The transfer function of the integrator A_{int} is given by (25). The DC gain is set by the ratio of the resistances R_3/R_2. The integrating time constant is set by the product $R_3 \times C_2$.

For noise analysis of the proposed system in Figure 4.5 is simplified to the system in Figure 4.6. The three electrode sensor model is reduced to a parallel RC circuit of R_1 and C_1. The first stage of any system is the dominant noise source. The gain of the I-V converter reduces the relative noise contributed by the multiplier and the integrator.

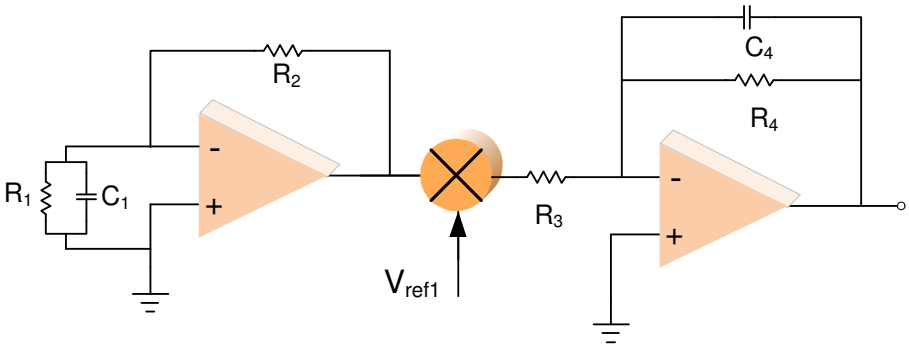

Figure 4.6 Proposed circuit with reduced sensor model for noise analysis.

Noise gain of I-V converter using reduced sensor model for analysis is

$$A_{noise} = 1 + \frac{R_2}{R_1}\left(sR_1C_1 + 1\right) \tag{26}$$

Op-amp noise includes thermal and flicker noise generated by the FET transistors. At low frequencies the flickr noise is more significant than thermal noise.

$$\begin{aligned} V_{n_{opamp1}}^2 &= V_{n_{th}}^2 + V_{n_f}^2 = 4kTR_{opamp}B + K_{opamp}\sqrt{\left(\ln\frac{f_c}{f_1}\right)} \\ &\approx K_{opamp}\sqrt{\left(\ln\frac{f_c}{f_1}\right)} \end{aligned} \tag{27}$$

Noise gain of the system now includes the gain of the multiplier Amul and integrator Aint

$$V_{n_{total}}^2 \approx V_{n_{opamp}1}^2 \bullet A_{noise}^2 = V_{n_{opamp}1}^2 \bullet \left(A_{I-V} \bullet A_{mul} \bullet A_{\text{int}}\right)^2 \quad (28)$$

Inserting the gain equation of I-V converter analyzed earlier and the integrator gain equation analyzed from the figure above, we get:

$$V_{n_{total}}^2 \approx V_{n_{opamp1}}^2 \bullet A_{noise}^2$$
$$= K_{opamp} \sqrt{\left(\ln \frac{f_c}{f_1}\right)} \bullet \left(\left(1+\frac{R_2}{R_1}\left(sR_1C_1+1\right)\right)(1)\left(\frac{R_4}{R_3}\left(\frac{1}{sR_4C_4+1}\right)\right)\right)^2 \quad (29)$$

After the equation is reduced, we see that by careful selection of R4 and C4 a pole-zero cancellation can be achieved to reduce the total noise.

$$V_{n_{total}}^2 \approx K_{opamp} \sqrt{\left(\ln \frac{f_c}{f_1}\right)} \bullet \left(\frac{R_2}{R_1}\frac{R_4}{R_3}\left(\frac{sR_1C_1+1}{sR_4C_4+1}\right)\right)^2 \quad (30)$$

4.2 PCB Implementation

A PCB prototype of the system is developed on a FR4 board. The integrated components used are SMT type and the passive components are DIP type for this implementation. The LTC2050 from linear technologies was chosen for the op-amp since it had a high gain and low offset with a dual power supply of ±2.5V. The multiplier chip from analog devices AD633 was one of the only four quadrant analog multiplier available commercially off the shelf. The micrcontroller board Arduino which has the Atmega 328 was used. The microcontroller contained a 10-bit 20 MHz analog-to-digital converter which was sufficient for the PCB prototype implementation.

Simulation is done using Cadence spectre simulator and using available spice models for the integrator components. Analog Correlator based system achieves linear output of 0.23V to 1.42V for 5uA to 30uA input as shown in Figure 4.7. Total noise is 65.31 uVrms.

Table 2. PCB components

Component	Company	Model No.
Op-Amp	Linear Technologies	LTC2050
Multiplier	Analog Devices	AD633
Microcontroller	Atmel	Atmega 328

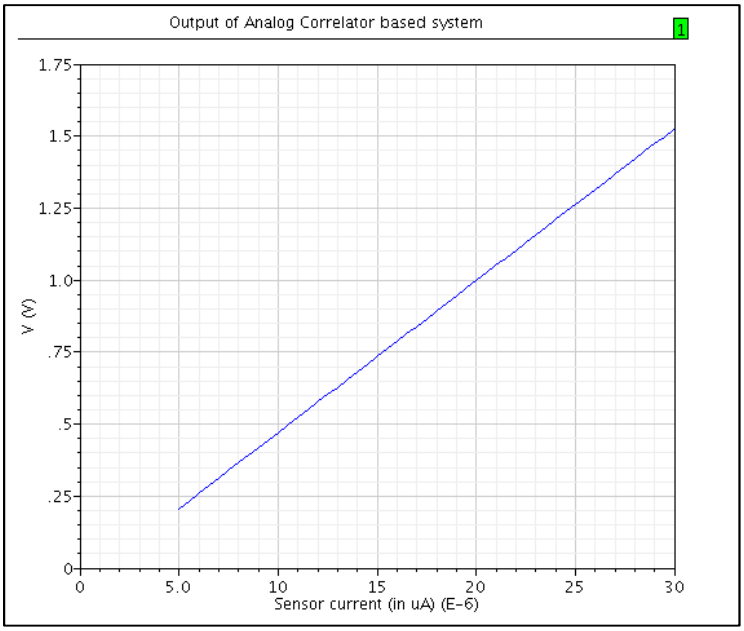

Figure 4.7 PCB prototype DC response

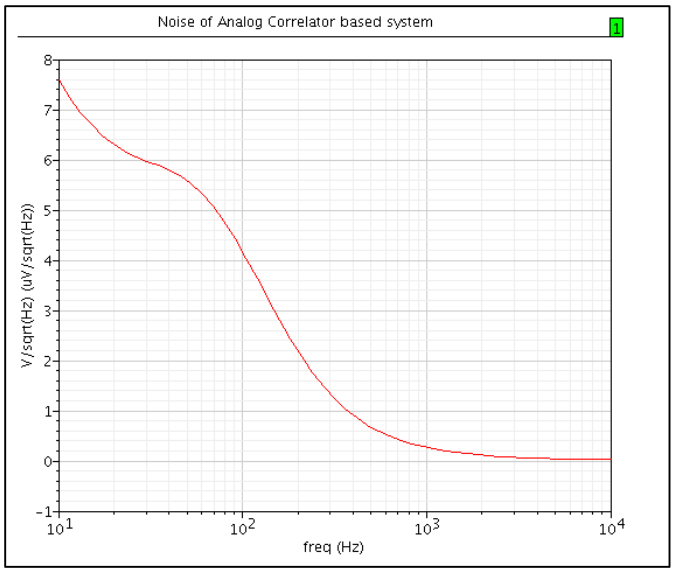

Figure 4.8 PCB prototype noise response

4.2.1Measurement Results

The top view of the PCB prototype is shown in Figure 4.9. The bottom view is shown in Figure 4.10. The measurement setup of the PCB prototype is shown in Figure 4.11.

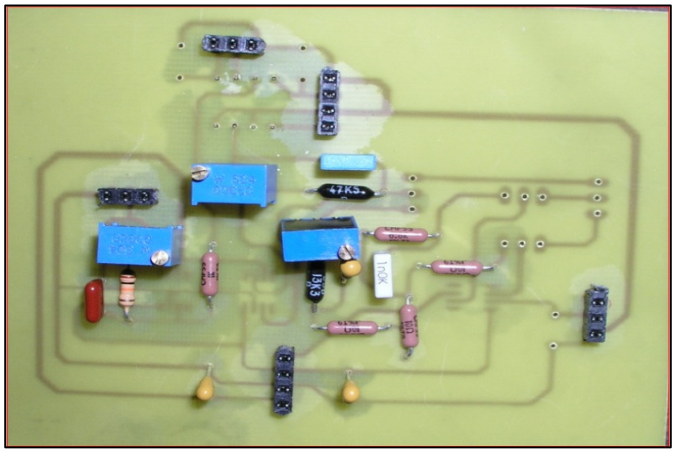

Figure 4.9 Top View of PCB for Analog Correlator type circuit

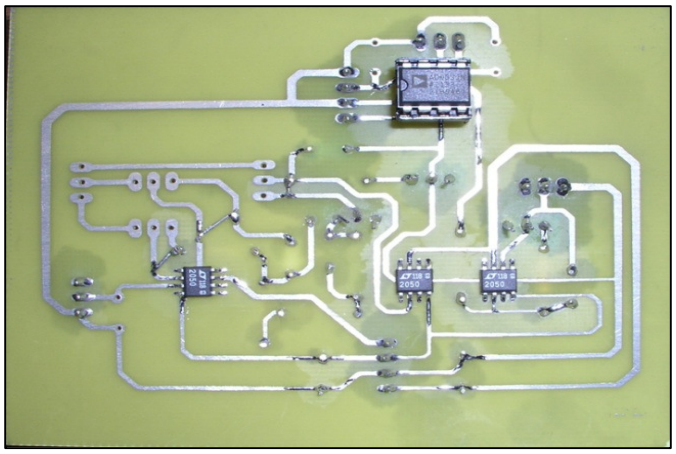

Figure 4.10 Bottom View of PCB for Analog Correlator type circuit

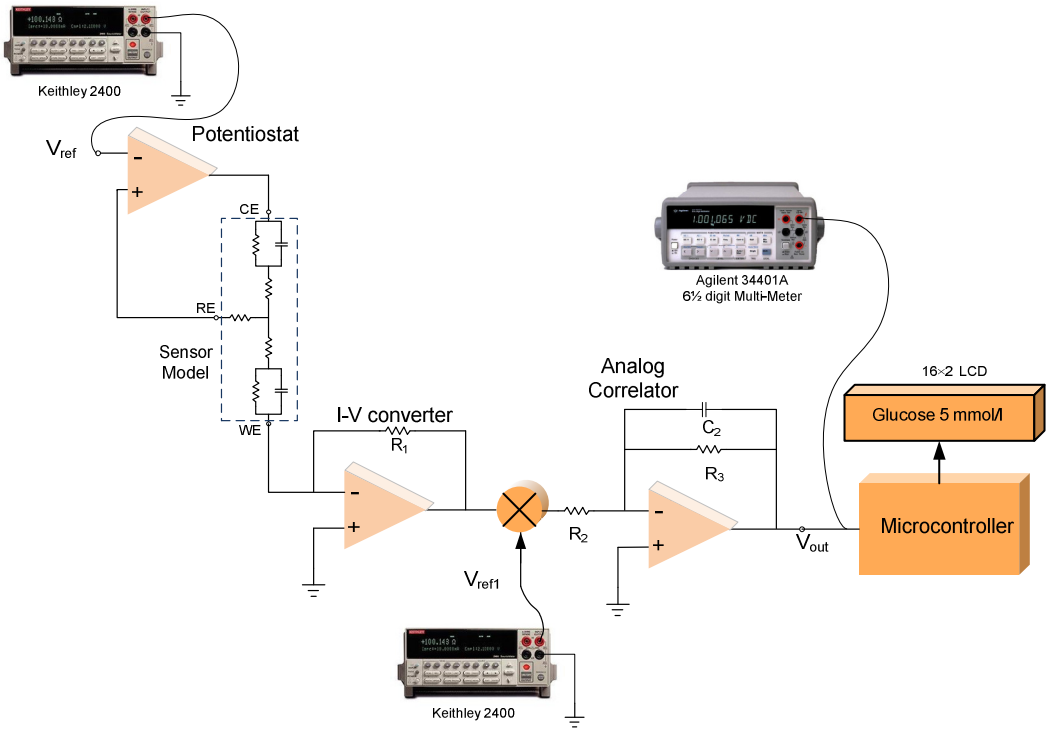

Figure 4.11 Measurement setup for the PCB prototype.

The comparison of simulated and measured output voltage is shown in Figure 4.12. The plot shows a fairly linear output with a slight offset due to the multiplier chip which can be corrected using the offset correction pin on the multiplier.

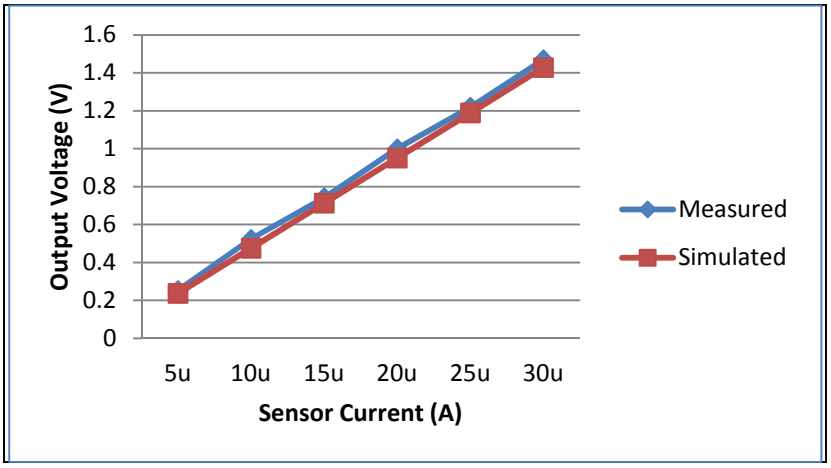

Figure 4.12 Comparison of Measurement and Simulated output voltage.

4.3 CMOS IC implementation

The proposed analog correlator based readout circuit is designed and implemented in 0.35um CMOS process. This section includes the design and analysis of the op-amp and the multiplier and the simulation and measurement results of the final integrated system.

4.3.1 Op-amp

The op-amp should achieve good linearity over the input range of 5uA to 30uA current generated by the micro-needle glucose sensor. The op-amp should also have high gain to reduce the gain error due to feedback. The telescope cascode op-amp provides very large gain due its cascode structure, but their output swings are relative limited due to overdrive voltages of the stacked transistors. Folded cascode op-amps provided relatively larger output swing while providing equally large gain as the telescopic op-amps [39]. The main disadvantage is it generally consumes higher power due the requirement of the additional bias current of the folded structure and also potentially suffers from greater noise. For this work, to achieve the primary goal of I-V conversion of

the full output current range of the micro-needle glucose sensor the folded cascode op-amp is chosen. Figure 4.13 shows the schematic of the folded cascode op-amp.

The op-amp is a differential-to-single ended type with NMOS input pairs. Due to their higher mobility the NMOS input pairs give higher gain and lower noise as compared to PMOS input pairs. To improve the output swing, a modified connection is made for the PMOS load instead of the typical diode connected cascode current mirror as seen in Figure 4.13.

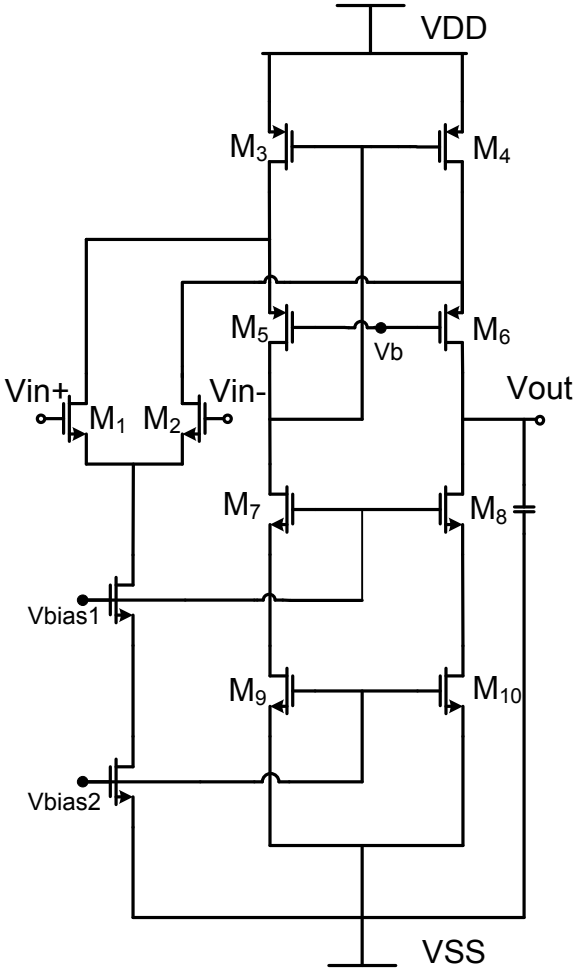

Figure 4.13 Folded cascode op-amp schematic.

The gain of the folded cascode op-amp schematic shown in Figure 4.13 is

$$A_v \approx g_{m1}\left(\left[(g_{m6}+g_{mb6})r_{o6}(r_{o2} \parallel r_{o4})\right] \parallel \left[(g_{m8}+g_{mb8})r_{o8}.r_{o10}\right]\right) \quad (31)$$

Proper biasing of the transistors at V_{bias1}, V_{bias2} and V_b in Figure 4.13 is critical to achieve minimum output voltages for the cascode current source loads, thereby giving high output swing. This is done by using a high-swing cascode current mirror shown in Figure 4.14.

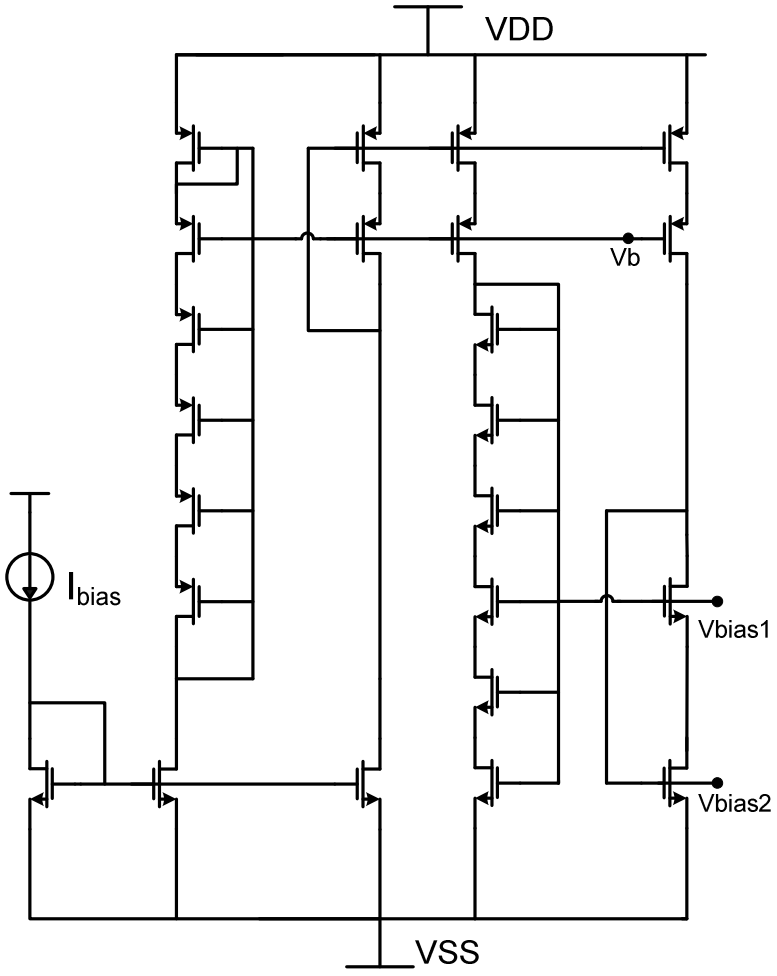

Figure 4.14 A high swing cascode current mirror for biasing

This is a modified Sooch cascode current mirror. The current source MOS transistors are minimally biased to operate at the edge of active region while the cascode

MOS transistors are in saturation [40]. This helps reduce the voltage headroom consumption by one threshold voltage which is significant. The minimum output voltage of the cascode current mirror shown in (32).

$$V_{out(\min)} = 2V_{ov} = 2\sqrt{\frac{2.I_D}{\mu C_{ox} W/L}} \tag{32}$$

The device dimensions of MOS transistors in the high swing cascode current mirror are chosen identical to the dimensions of the MOS transistors in the op-amp to minimize the mismatch introduced due to process variation.

To achieve the full output swing over a load, a large current-driving output stage is is required. The output stage schematic shown in Figure 4.15 is a buffer amplifier which is a typical two-stage differential-to-single ended circuit at its core. This schematic uses a negative feedback by shorting the output of the buffer amplifier to its negative input. This gives the output stage a very low output resistance and helps drive large loads. The output resistance of the schematic in Figure 4.15 is

$$\mathrm{R_{out}} = \left(\frac{1}{(\mathrm{g_{ds6}} + \mathrm{g_{ds7}})\left[1 + \left(\frac{\mathrm{g_{m2}}}{2\mathrm{g_{m4}}}\right)\left(\frac{\mathrm{g_{m6}} + \mathrm{g_{m7}}}{\mathrm{g_{ds6}} + \mathrm{g_{ds7}}}\right)\right]} \right) \tag{33}$$

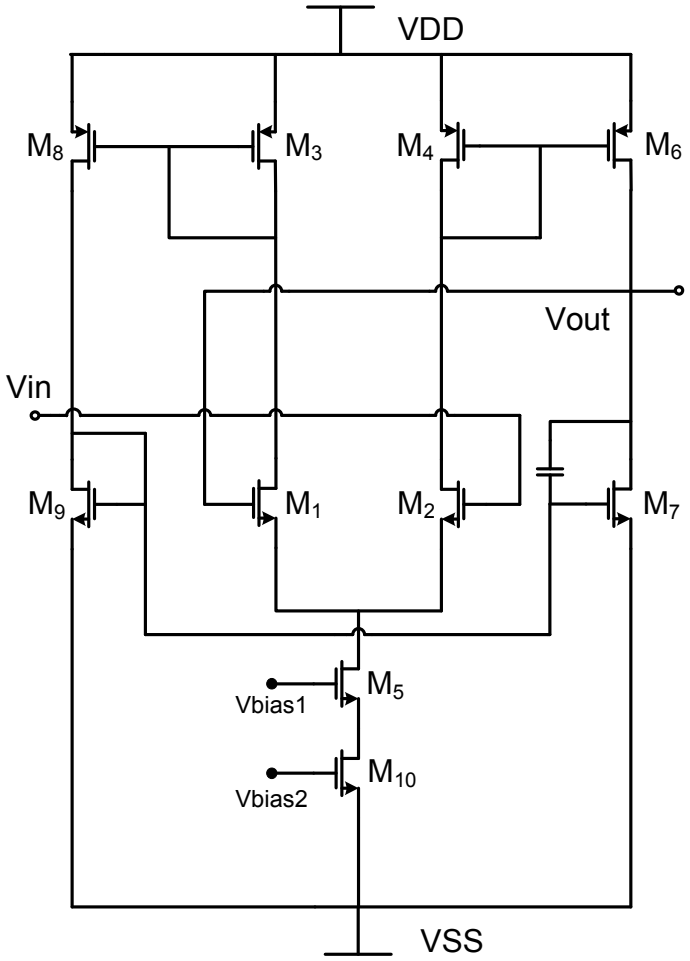

Figure 4.15 Output buffer stage

Op-amp noise analysis

Due to the demand for high sensitivity in the current readout circuit, care has been taken to minimize the noise power due to the amplifiers. In the noise analysis of these amplifiers, only devices in the signal path are important and noise in the cascode devices can be ignored. Also, noise contribution of the tail current source transistors is cancelled by the differential symmetry and matching. The resulting input referred noise spectrum of the amplifier can be expressed as

$$\overline{v_{n,tot}^2} = 2\left[\overline{v_{n1}^2}(f) + \left(\frac{g_{m3}}{g_{m1}}\right)^2 \overline{v_n^3}(f) + \left(\frac{g_{m9}}{g_{m1}}\right)^2 \overline{v_9^2}(f)\right] \quad (34)$$

where $\overline{v_{ni}^2}(f)$ represents the noise spectral corresponding to the i^{th} transistor due to both thermal and 1/f component and g_{mi} is the transconductance of transistor M_i. Substituting the thermal noise and 1/f noise of M1, M3, and M9 into the input voltage noise spectral yields,

$$\overline{v_{n,tot}^2} = \frac{16kT}{3\sqrt{2\mu_n C_{ox}\left(W/L\right)_1 I_{DS1}}}\left(1 + \sqrt{\frac{2\mu_p\left(W/L\right)_3}{\mu_n\left(W/L\right)_1}} + \sqrt{\frac{\left(W/L\right)_9}{\left(W/L\right)_1}}\right) + \frac{2k_{fn}}{C_{ox}(WL)_1}\frac{\Delta f}{f}\left[1 + \frac{2\mu_p k_{fp}}{\mu_n k_{fn}}\left(\frac{L_1}{L_3}\right)^2 + \left(\frac{L_1}{L_9}\right)^2\right] \quad (35)$$

This equation shows that an increasing W/L for the input devices and increasing the tail current will decrease the thermal noise. Since $\mu_n > \mu_p$, the amplifier with NMOS inputs has less thermal noise than one with PMOS input devices. The noise contributed by the output stage is

$$\overline{v_{n,tot}^2} = \frac{16kT}{3}\frac{1}{g_{m1}^2}\left[g_{m1} + g_{m3} + \frac{g_{m8} + g_{m9}}{g_{m8}^2(r_{01} \| r_{03})^2}\right] \quad (36)$$

$$\approx \frac{16kT}{3\sqrt{2\mu_n C_{ox}\left(\frac{W}{L}\right)_1 \frac{I_{ss}}{2}}}\left\{1 + \sqrt{\frac{\mu_p\left(\frac{W}{L}\right)_3}{\mu_n\left(\frac{W}{L}\right)_1}}\right\} + \frac{2k_{fn}}{C_{ox}(WL)_1}\frac{1}{f}\left[1 + \frac{\mu_p k_{fp}}{\mu_n k_{fn}}\left(\frac{L_1}{L_3}\right)^2\right] \quad (37)$$

From (37), it is seen that to reduce the noise decreases with decrease in PMOS transistor width to length ratio and increase in NMOS transistor width to length ratio.

The final complete schematic is shown in Figure 4.16.

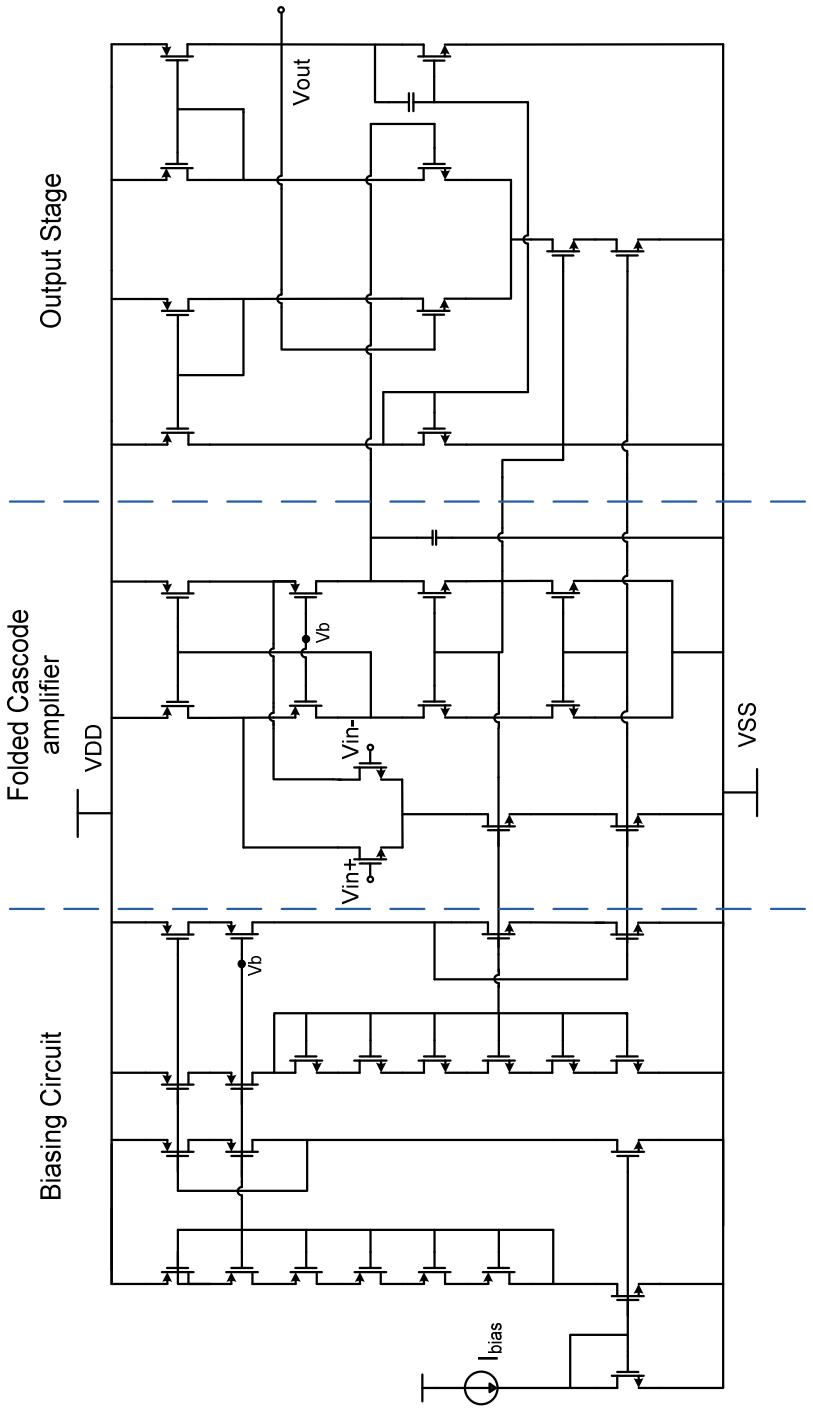

Figure 4.16 Complete Op-amp Schematic

Figure 4.17 shows in the op-amp gain and phase plot. The op-amp achieves a 118.3 dB gain and 47.3 degrees phase margin for a load capacitance of 100fF.

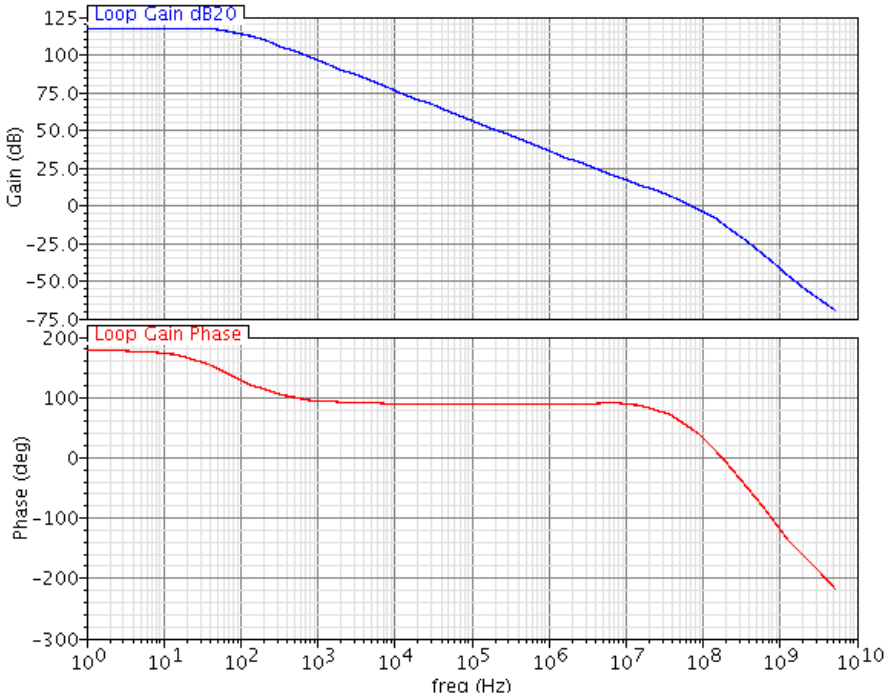

Figure 4.17 Op-amp Gain and Phase plot

To measure the output and input swing, the op-amp was simulated with unity-gain buffer configuration by shorting the output with the negative input. The positive input was swept with a DC Voltage from VDD to VSS. The output vs input curve is shown in Figure 4.18. The output swing of 1.56 to -1.52V is achieved.

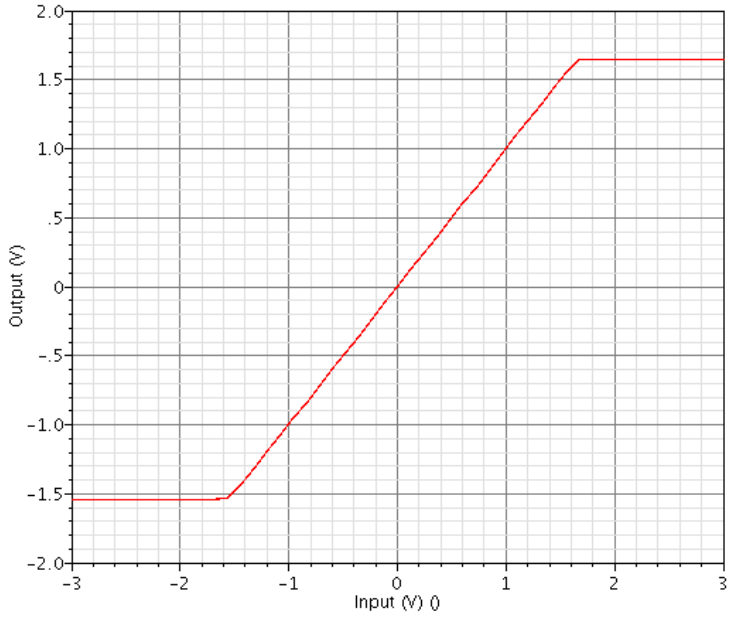

Figure 4.18 Op-amp DC response

4.3.2 Multiplier

The analog multiplier for the correlator can be realized using the Gilbert cell architecture. This circuit is widely used in many analog and communication systems. The schematic in Figure 4.19 shows analog multiplier schematic with three differential NMOS pairs and diode-connected PMOS loads. Two of the NMOS differential pairs at the top have x input and the bottom differential pair has y input. The tail current source used in the standard Gilbert cell is not used here to improve output swing.

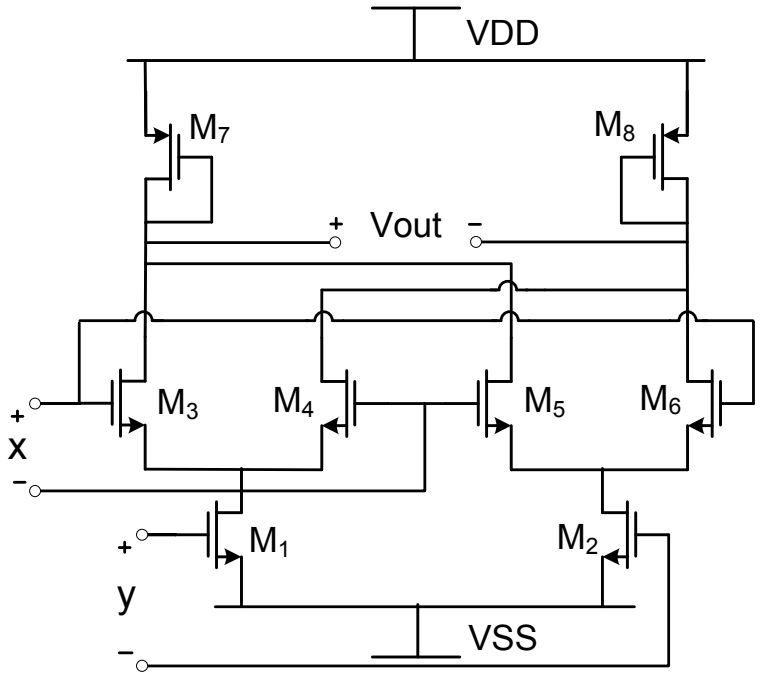

Figure 4.19 Gilbert cell analog multiplier.

In this type of multiplier which works on the principle of square law of MOS transistors and cancellation achieved by this method is given by following equations.

$$I_{out} = (I_3 + I_5) - (I_4 + I_6) \tag{38}$$

$$= (I_3 - I_4) - (I_6 - I_5) \tag{39}$$

Substituting the square-law current equation for the two differential pairs M_3-M_4 and M_6-M_5 with I_{y1} and I_{y2} as their respective tail currents into (39), we get

$$= kV_x\sqrt{\frac{2I_{y_1}}{k} - V_x^2} - kV_x\sqrt{\frac{2I_{y_2}}{k} - V_x^2} \tag{40}$$

$$= \mathrm{kV_x}\sqrt{\frac{2}{\mathrm{k}}\left(\mathrm{k}\frac{\mathrm{V_y}}{2} - \mathrm{V_t}\right)^2 - \mathrm{V_x^2}} - \mathrm{kV_x}\sqrt{\frac{2}{\mathrm{k}}\left(\mathrm{k} - \frac{\mathrm{V_y}}{2} - \mathrm{V_t}\right)^2 - \mathrm{V_x^2}} \tag{41}$$

Assuming V_x is small

$$= \sqrt{2}kV_x\left\{\sqrt{\left(\frac{V_y}{2} - V_t\right)^2} - \sqrt{\left(\frac{-V_y}{2} - V_t\right)^2}\right\} \quad (42)$$

$$= \sqrt{2}kV_xV_y \quad (43)$$

To see the input linear range of the multiplier, the output versus input curve of the multiplier was plotted by sweeping the 'y' input of the multiplier from Vdd to Vss and a parametric sweep of 'x' for three values. Figure 4.20 shows the multiplier response in four quadrants. The multiplier achieves a sufficient linear range of an 'y' input of -0.5V to 0.5V and gives maximum gain when 'x' input is 1V or more.

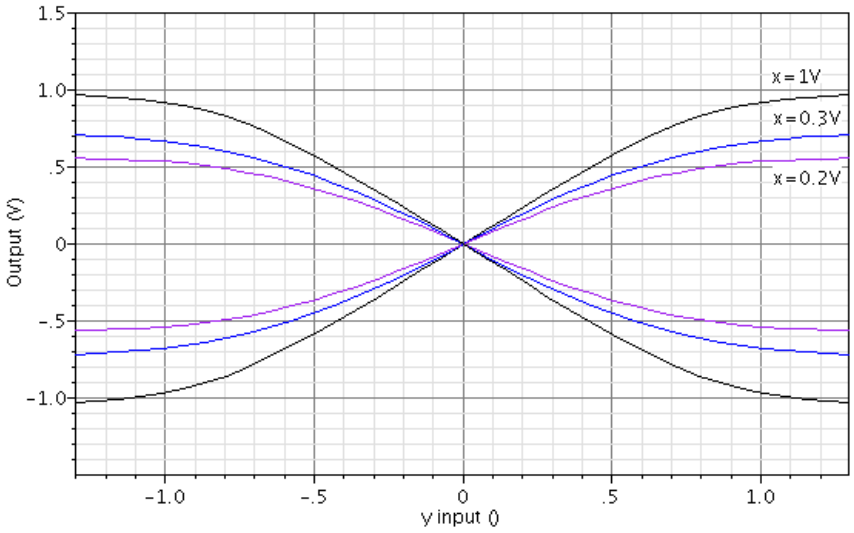

Figure 4.20 The Multiplier four quadrant simulation.

Multiplier noise analysis

The multiplier total noise comes from three main sources, the noise from the four NMOS transistors with x input, the two NMOS transistors with y input and the two PMOS load transistors.

$$\overline{v_n^2} = \left\{4\overline{i_{nx}^2} + 2\overline{i_{ny}^2} + 2\overline{i_{np}^2}\right\}\frac{1}{g_{mp}^2} \tag{44}$$

Each transistor contributes a thermal and flickr noise. Substituting for the thermal noise and flickr noise into (44), we get

$$\begin{aligned}\overline{v_n^2} &= \frac{16}{3}kT\left\{\frac{2g_{mx}+g_{my}}{g_{mp}^2}+\frac{1}{g_{mp}}\right\} \\ &\quad + \frac{2K_{fp}}{C_{ox}f\left(W/L\right)_p}\left\{\frac{K_{fn}}{K_{fp}}\frac{\mu_n}{\mu_p}\left\{2\left(\frac{L_p}{L_x}\right)^2+\frac{1}{2}\left(\frac{L_p}{L_y}\right)^2\right\}+1\right\}\end{aligned} \tag{45}$$

$$\begin{aligned}&\approx \frac{16kT}{3\sqrt{2\mu_p C_{ox}\left(\frac{W}{L}\right)_p I}}\left\{1+\sqrt{\frac{2\mu_n\left(\frac{W}{L}\right)_x}{\mu_p\left(\frac{W}{L}\right)_p}}+\sqrt{\frac{\mu_n\left(\frac{W}{L}\right)_y}{\mu_p\left(\frac{W}{L}\right)_p}}\right\} \\ &\quad + \frac{2K_{fp}}{C_{ox}f\left(W/L\right)_p}\left\{\frac{K_{fn}}{K_{fp}}\frac{\mu_n}{\mu_p}\left\{2\left(\frac{L_p}{L_x}\right)^2+\frac{1}{2}\left(\frac{L_p}{L_y}\right)^2\right\}+1\right\}\end{aligned} \tag{46}$$

From (46), it is seen that to reduce the noise decreases with increase in PMOS transistor width to length ratio and decrease in NMOS transistor width to length ratio.

4.3.3 Simulation Results

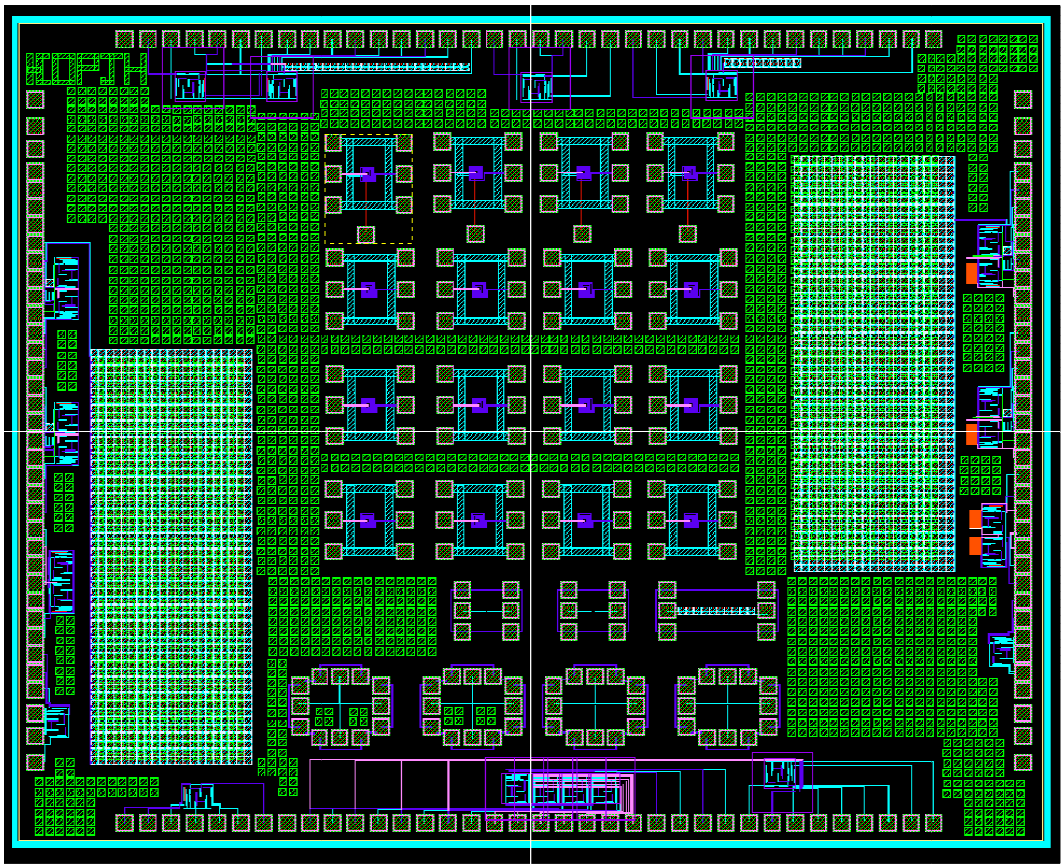

Figure 4.21 Complete chip layout screen shot.

The proposed circuit is fabricated in 0.35um CMOS process. Cadence virtuoso tool was used for schematic and layout routing. Assura was used for the DRC check, LVS check and RC extraction of the layout. The PAD size is 81.4um × 81.4um. The total area of the proposed readout circuit is 300um × 167um.

The system DC response for input range of 5uA to 30uA is shown in Figure 4.22. The output range is from 300mV to 1.24V and is linear. Figure 4.23 shows the noise response of the system from 10Hz to 100MHz. The total output rms noise is simulated to be 5.3mV_{rms}.

Figure 4.22 Analog Correlator based readout circuit DC response

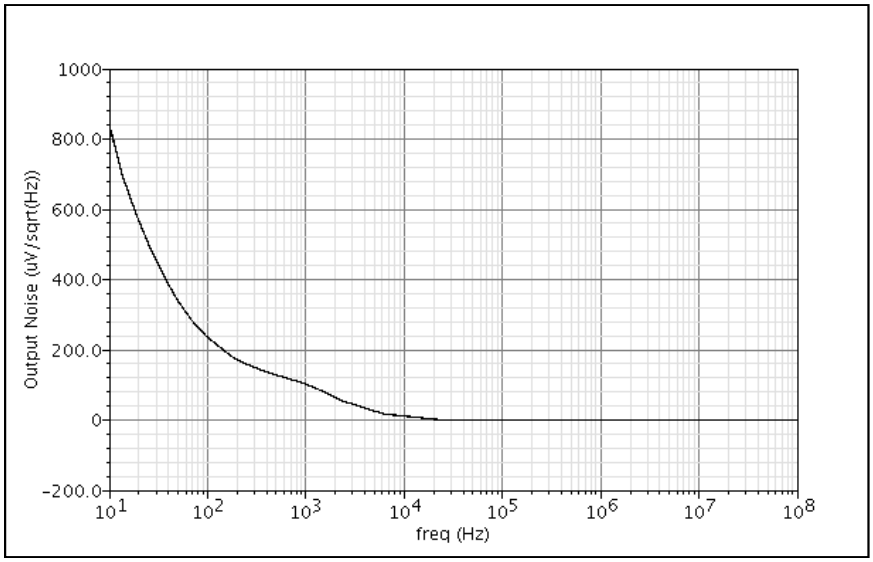

Figure 4.23 Analog Correlator based readout circuit noise response

4.3.4 Measurement Results

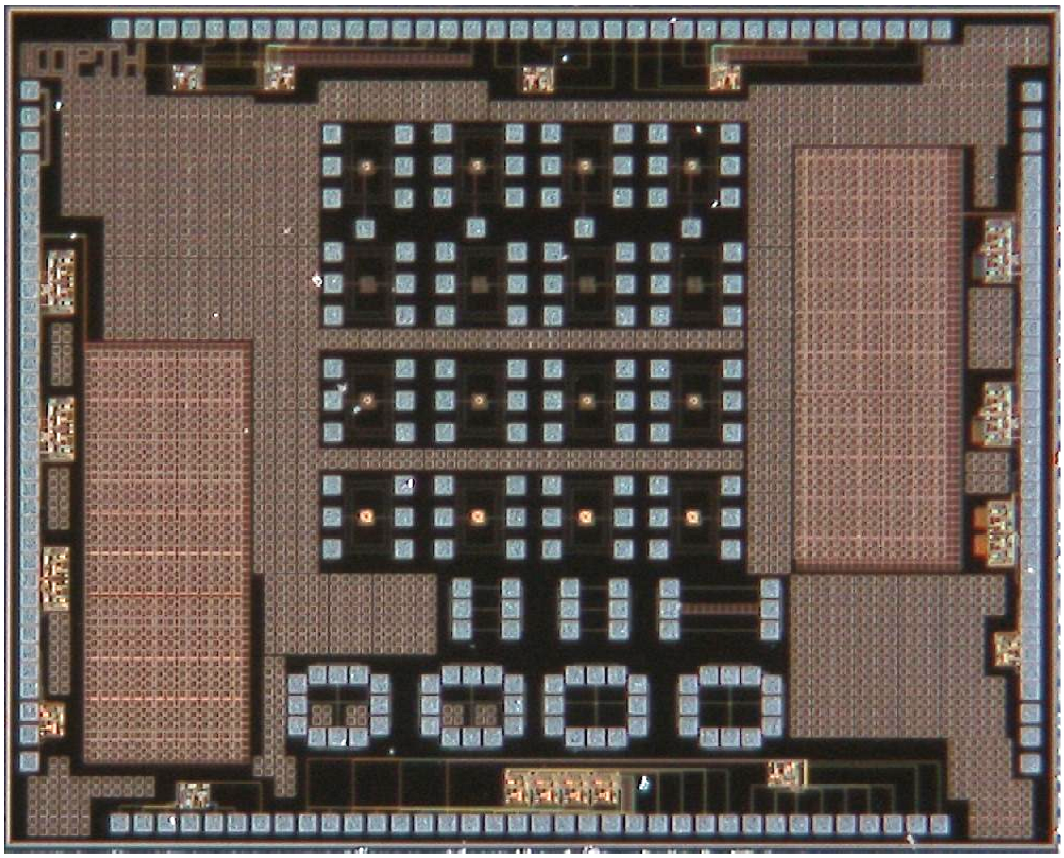

Figure 4.24 Chip photo.

The chip photo containing the analog correlator based readout circuit fabricated in 0.35um CMOS process is shown in Figure 4.24. The measurement setup is shown in Figure 4.25. The package chip is tested using an adapter board. Keithley 2400 source-meters are used to provide input current and bias current to the readout circuit and an Agilent 34401A multi-meter is used to read the output of the readout circuit.

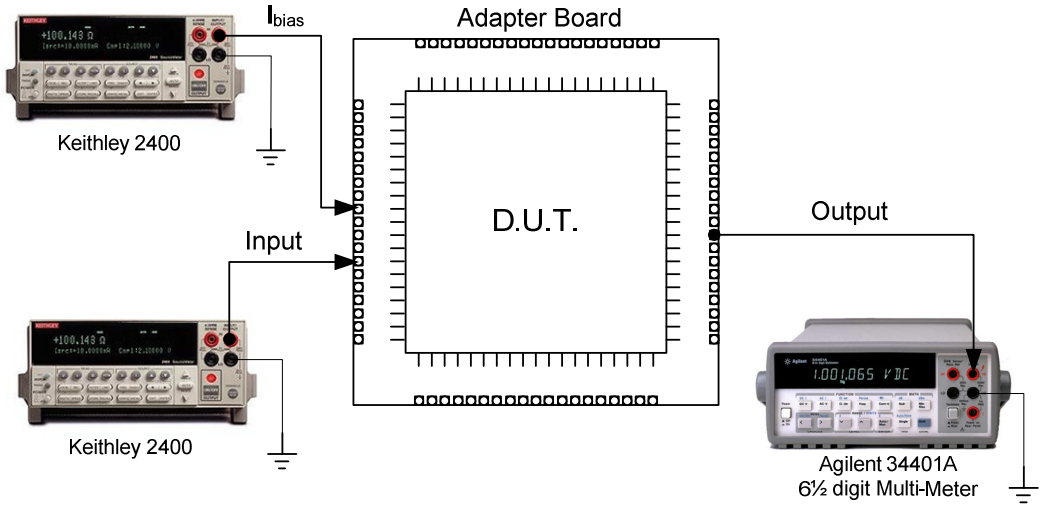

Figure 4.25 Measurement setup for DC response

Figure 4.26 shows the DC response of the Correlator system. The measurement result shows a good match with the simulation result. To compare the linearity, the dashed plots in Figure 4.26 represent the ideal response for the particular gain. The error between the result plot and ideal plot is computed at 5 data points shown in Table 3.

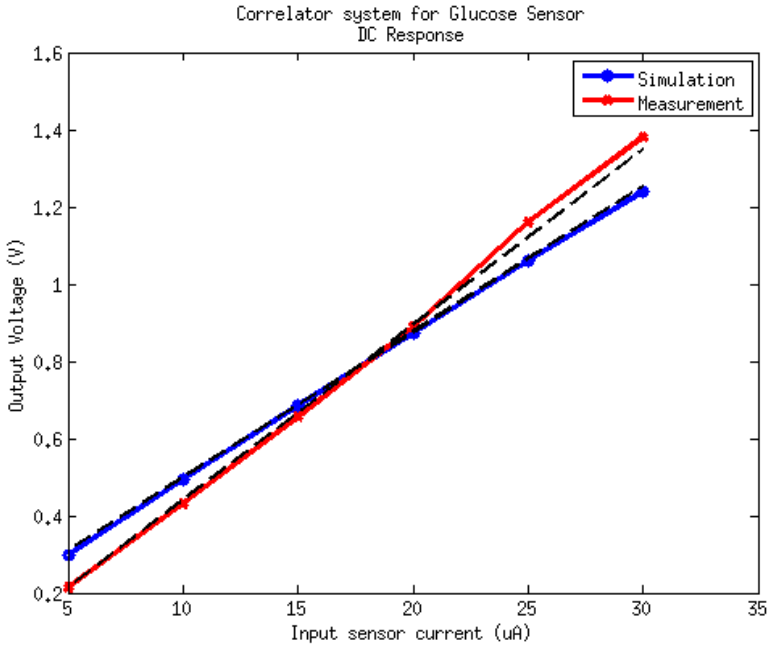

Figure 4.26 Output vs. Input measurement for analog correlator based readout circuit.

Table 3 Output Voltage and Error (%) of analog correlator based readout circuit

Input Sensor Current (A)	Simulation		Measurement	
	Output Voltage (V)	Error (%)	Output Voltage (V)	Error (%)
5u	0.29	3.59	0.21	0
10u	0.49	1.06	0.43	2.27
15u	0.68	0.33	0.65	1.49
20u	0.87	0.26	0.89	0.44
25u	1.06	0.51	1.16	3.47
30u	1.24	1.08	1.38	2.37

To measure the output noise, the input is grounded and the output is read through a digital storage oscilloscope. The screenshot of the oscilloscope with the output noise is shown in Figure 4.27. Using the RMS measurement feature of the oscilloscope, the total output noise is measured to be 6.60 mV_{rms}.

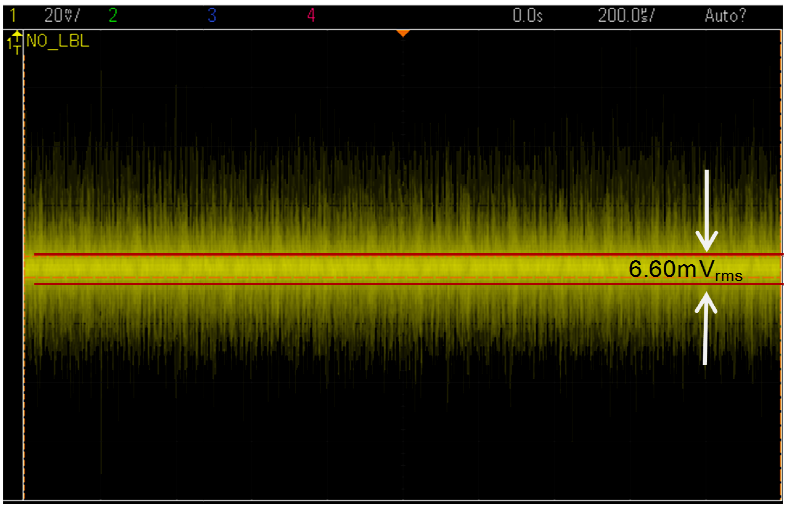

Figure 4.27 Oscilloscope screenshot for output noise measurement

Table 4 summarizes the measurement results of the proposed analog correlator based readout circuit.

Table 4 Summary of measurement results

Parameters	Measurement result
Range	5uA-30uA
Noise	6.6mV$_{rms}$
Mean Error	1.6%
Gain	44.3kΩ
Power	5.1mW

Chapter 5

Conclusion

In this work, an analog correlator based readout circuit for amperometric glucose electrochemical biosensors is proposed. It is designed to work with the output range of a novel microneedle based non-enzymatic painless glucose sensor [12]. This minimally invasive sensor is designed to measure the glucose level of the interstitial fluid in epidermis layer. The analog correlator based readout circuit can achieve the required input current range (5µA to 30µA) from the microneedle based glucose sensor and show a linear output in that range. The analog correlator based glucose sensor readout circuit offers lower noise and wider dynamic range compared to the conventional TIA architecture and is a better solution for the readout circuit for the microneedle based sensor. This complete circuit is implemented in two different ways: first a PCB implementation and then a CMOS integrated circuit implementation.

In the PCB implementation, the circuit is designed using COTS SMD components on an FR4 board. It is tested with a three-electrode electrochemical glucose sensor model implemented in passive components. The measurement results show that the COTS system of functions in the sensor current range of 5µA to 30µA giving a linear output range of 0.23V to 1.42V. Hence the PCB implementation can be successfully interfaced with a microneedle based glucose sensor.

In the CMOS integrated circuit implementation, the analog correlator based readout circuit is designed and fabricated in 0.35um CMOS process. The individual components include the op-amp and multiplier. The op-amp is folded cascode structure at the core to provide a high gain and the output stage is two stage differential-to-single ended amplifier with negative feedback to provide a wide output range. The op-amp

achieves a 118.3 dB gain and 47.3 degrees phase margin. The multiplier is realized using a four quadrant Gilbert cell circuit. The PAD size is 81.4um × 81.4um. The total area of the proposed readout circuit is 300um × 167um. The circuit DC response for input range of 5uA to 30uA gives a linear output voltage range from 0.21V to 1.38V and is linear. The total output RMS noise is simulated to be 6.6mV_{RMS}. The circuit has an accuracy of 1.6% and consumes 5.1mW of power. The analog correlator based glucose sensor readout circuit is proved to have lower noise performance and wider dynamic range as opposed to the conventional TIA architecture.

For future work, it is intended to integrate the CMOS integrated readout circuit with the microneedle based glucose sensor to form a more compact, cheaper and minimally invasive solution to existing methods of commercially available glucose sensing products. This would a diabetes patients a more painless and cost-effective solution to monitor their glucose levels and help improve their health overall.

References

[1] "Diabetes Type 1." [Online]. Available: http://www.nlm.nih.gov/medlineplus/diabetestype1.html. [Accessed: 06-Apr-2013].

[2] S. Wild, G. Roglic, A. Green, R. Sicree, and H. King, "Global prevalence of diabetes: estimates for the year 2000 and projections for 2030," *Diabetes Care*, vol. 27, no. 5, pp. 1047–1053, May 2004.

[3] C. C. Cowie, K. F. Rust, D. D. Byrd-Holt, E. W. Gregg, E. S. Ford, L. S. Geiss, K. E. Bainbridge, and J. E. Fradkin, "Prevalence of diabetes and high risk for diabetes using A1C criteria in the U.S. population in 1988-2006," *Diabetes Care*, vol. 33, no. 3, pp. 562–568, Mar. 2010.

[4] J. E. Shaw, R. A. Sicree, and P. Z. Zimmet, "Global estimates of the prevalence of diabetes for 2010 and 2030," *Diabetes Res. Clin. Pract.*, vol. 87, no. 1, pp. 4–14, Jan. 2010.

[5] D. D. Cunningham and J. A. Stenken, Eds., *In Vivo Glucose Sensing, Volume 174*. 2009.

[6] N. S. Oliver, C. Toumazou, A. E. G. Cass, and D. G. Johnston, "Glucose sensors: a review of current and emerging technology," *Diabetic Medicine*, vol. 26, no. 3, pp. 197–210, 2009.

[7] M. S. Boyne, D. M. Silver, J. Kaplan, and C. D. Saudek, "Timing of changes in interstitial and venous blood glucose measured with a continuous subcutaneous glucose sensor," *Diabetes*, vol. 52, no. 11, pp. 2790–2794, Nov. 2003.

[8] V. Thomé-Duret, G. Reach, M. N. Gangnerau, F. Lemonnier, J. C. Klein, Y. Zhang, Y. Hu, and G. S. Wilson, "Use of a subcutaneous glucose sensor to

detect decreases in glucose concentration prior to observation in blood," *Anal. Chem.*, vol. 68, no. 21, pp. 3822–3826, Nov. 1996.

[9] S. Gebhart, M. Faupel, R. Fowler, C. Kapsner, D. Lincoln, V. McGee, J. Pasqua, L. Steed, M. Wangsness, F. Xu, and M. Vanstory, "Glucose sensing in transdermal body fluid collected under continuous vacuum pressure via micropores in the stratum corneum," *Diabetes Technol. Ther.*, vol. 5, no. 2, pp. 159–166, 2003.

[10] K. Tsuchiya, N. Nakanishi, Y. Uetsuji, and E. Nakamachi, "Development of blood extraction system for health monitoring system," *Biomed Microdevices*, vol. 7, no. 4, pp. 347–353, Dec. 2005.

[11] W. H. Smart and K. Subramanian, "The use of silicon microfabrication technology in painless blood glucose monitoring," *Diabetes Technol. Ther.*, vol. 2, no. 4, pp. 549–559, 2000.

[12] Y. Yoon, J. Kim, K. Lee, H. Song, K. Yoo, G. Lee, and J. Lee, "A novel microneedle-based non- enzymatic glucose sensor for painless diabetes testing application," in *Solid-State Sensors, Actuators and Microsystems Conference (TRANSDUCERS), 2011 16th International*, 2011, pp. 2164–2167.

[13] N. Kakehi, T. Yamazaki, W. Tsugawa, and K. Sode, "A novel wireless glucose sensor employing direct electron transfer principle based enzyme fuel cell," *Biosens Bioelectron*, vol. 22, no. 9–10, pp. 2250–2255, Apr. 2007.

[14] S. Zimmermann, D. Fienbork, A. W. Flounders, and D. Liepmann, "In-device enzyme immobilization: wafer-level fabrication of an integrated glucose sensor," *Sensors and Actuators B: Chemical*, vol. 99, no. 1, pp. 163–173, Apr. 2004.

[15] K. Kim and J.-B. Lee, “High aspect ratio tapered hollow metallic microneedle arrays with microfluidic interconnector,” *Microsyst. Technol.*, vol. 13, no. 3, pp. 231–235, Dec. 2006.

[16] A. J. Bard and L. R. Faulkner, *Electrochemical Methods: Fundamentals and Applications*. Wiley, 2001.

[17] J. T. Maloy, “Factors Affecting the Shape of Current-Potential Curves.,” *Journal of Chemical Education*, vol. 60, no. 4, pp. 285–89, Apr. 1983.

[18] U. Guth, W. Vonau, and J. Zosel, “Recent developments in electrochemical sensor application and technology—a review,” *Meas. Sci. Technol.*, vol. 20, no. 4, p. 042002, Apr. 2009.

[19] B. R. Eggins, Ed., *Analytical Techniques in the Sciences: Chemical Sensors and Biosensors*. 2007.

[20] S. Hwang, *Integrated Cmos Microsystems for Electrochemical Sensing*. BiblioBazaar, 2011.

[21] E. Wilkins and P. Atanasov, “Glucose monitoring: state of the art and future possibilities,” *Med Eng Phys*, vol. 18, no. 4, pp. 273–288, Jun. 1996.

[22] M. M. Ahmadi, *A Wireless Implantable Microsystem for Continuous Blood Glucose Monitoring*. University of Calgary (Canada), 2007.

[23] W. Zhang and G. Li, “Third-generation biosensors based on the direct electron transfer of proteins,” *Anal Sci*, vol. 20, no. 4, pp. 603–609, Apr. 2004.

[24] S. Park, H. Boo, and T. D. Chung, “Electrochemical non-enzymatic glucose sensors,” *Analytica Chimica Acta*, vol. 556, no. 1, pp. 46–57, Jan. 2006.

[25] J. Y. Park, Y. H. Kim, A. Seong, and Y. J. Yoo, “Amperometric determination of glucose, based on the direct electron transfer between glucose oxidase and tin oxide,” *Biotechnol Bioproc E*, vol. 13, no. 4, pp. 431–435, Aug. 2008.

[26] U. Gebhardt, G. Luft, G. J. Richter, and F. von Sturm, “253 - Development of an Implantable Electrocatalytic Glucose Sensor,” *Bioelectrochemistry and Bioenergetics*, vol. 5, no. 4, pp. 607–624, 1978.

[27] R. G. C. Kathryn E Toghill, “Electrochemical Non-enzymatic Glucose Sensors: A Perspective and an Evaluation,” *Int. J. Electrochem. Sci. International Journal*, vol. 5, pp. 1246–1301, 2010.

[28] D. Pletcher, “Electrocatalysis: present and future,” *Journal of Applied Electrochemistry*, vol. 14, no. 4, pp. 403–415, Jul. 1984.

[29] W. Schuhmann, “Biosensors: Microelectrochemical devices. By M. Lambrechts and W. Sansen, Institute of Physics Publishing, Bristol 1992, 304 pp., hardcover, £ 52, ISBN 0-7503-0112-0,” *Advanced Materials*, vol. 5, no. 10, pp. 771–772, 1993.

[30] D. T. Sawyer, *Electrochemistry for Chemists*. Wiley, 1995.

[31] J.-S. Y. Su-Moon Park, “Electrochemical impedance spectroscopy for better electrochemical measurements.,” *Analytical chemistry*, vol. 75, no. 21, p. 455A–461A, 2003.

[32] S. S. Taylor and T. P. Thomas, “A 2pA/ radic;Hz 622 Mb/s GaAs MESFET transimpedance amplifier,” in *Solid-State Circuits Conference, 1994. Digest of Technical Papers. 41st ISSCC., 1994 IEEE International*, 1994, pp. 254–255.

[33] K. Iniewski, *VLSI Circuits for Biomedical Applications*. Artech House, 2008.

[34] B. Razavi, “A 622 Mb/s 4.5 pA/ radic;Hz CMOS transimpedance amplifier [for optical receiver front-end],” in *Solid-State Circuits Conference, 2000. Digest of Technical Papers. ISSCC. 2000 IEEE International*, 2000, pp. 162–163, 453.

[35] R. Greef, “Instruments for use in electrode process research,” *J. Phys. E: Sci. Instrum.*, vol. 11, no. 1, p. 1, Jan. 1978.

[36] Jichun Zhang, N. Trombly, and A. Mason, “A low noise readout circuit for integrated electrochemical biosensor arrays,” in *Proceedings of IEEE Sensors, 2004*, 2004, pp. 36– 39 vol.1.

[37] Jichun Zhang, Yue Huang, N. Trombly, Chao Yang, and A. Mason, “Electrochemical array microsystem with integrated potentiostat,” in *2005 IEEE Sensors*, 2005.

[38] Y. YOON, “HIERARCHICAL MICRO/NANO STRUCTURES FOR PAINLESS GLUCOSE SENSOR AND SELF-CLEANING SURFACE APPLICATION,” The University of Texas at Dallas, 2013.

[39] B. Razavi, *Design of Analog CMOS Integrated Circuits*. McGraw-Hill Education, 2000.

[40] P. R. Gray, P. J. Hurst, and S. H. Lewis, *Analysis and Design of Analog Integrated Circuits*. Wiley, 2009.

[41] R. G. Kakerow, H. Kappert, E. Spiegel, and Y. Manoli, “Low-power Single-chip CMOS Potentiostat,” in *The 8th International Conference on Solid-State Sensors and Actuators, 1995 and Eurosensors IX.. Transducers ’95*, 1995, vol. 1, pp. 142–145.

[42] B. Goldstein, D. Kim, A. Rottigni, J. Xu, T. K. Vanderlick, and E. Culurciello, “CMOS low current measurement system for biomedical applications,” in *2011 IEEE International Symposium on Circuits and Systems (ISCAS)*, 2011, pp. 1017–1020.

[43] D. Kim, W. Tang, B. Goldstein, P. Weerakoon, H. Montanaro, B. Martini, and E. Culurciello, “Performance comparison of low current measurement systems for biomedical applications,” in *Proceedings of 2010 IEEE International Symposium on Circuits and Systems (ISCAS)*, 2010, pp. 3469–3472.

[44] R. Schreier, J. Silva, J. Steensgaard, and G. C. Temes, “Design-oriented estimation of thermal noise in switched-capacitor circuits,” *IEEE Transactions on Circuits and Systems I: Regular Papers*, vol. 52, no. 11, pp. 2358–2368, 2005.

[45] K. K. Hung, P.-K. Ko, C. Hu, and Y. C. Cheng, “A physics-based MOSFET noise model for circuit simulators,” *IEEE Transactions on Electron Devices*, vol. 37, no. 5, pp. 1323–1333, 1990.

[46] P. E. Allen and D. R. Holberg, *CMOS analog circuit design*. Holt, Rinehart and Winston, 1987.

[47] D. Binkley, *Tradeoffs and Optimization in Analog CMOS Design*. John Wiley & Sons, 2008.

[48] R. Gregorian, *Introduction to CMOS OP-AMPs and comparators*. Wiley, 1999.

Biographical Information

Varun Shenoy is a candidate for the Doctoral degree in Electrical Engineering at The University of Texas at Arlington. He received his Bachelor's degree in Electrical and Electronics Engineering from Manipal Institute of Technology, India. He later received his Master's degree in Electrical Engineering from The University of Texas at Arlington by completing his Master's Thesis under Dr. Sungyong Jung.

He joined the AMIC Design Lab and started his Ph.D. under the supervision of Dr. Sungyong Jung in Fall 2007. His research interests include Analog/RF CMOS integrated circuits and systems. He worked on several projects including time-reversal system for wireless transceivers, CMOS low noise amplifier design for short range automotive UWB radar receiver, and CMOS readout circuits for amperometric electrochemical sensors such as glucose sensors and nano-wire sensors.